Thermal resistance between metallic surfaces in different configurations for high current HTS Cable-in-Conduit Conductor

Master's Thesis of

Simone Severo

at the Institute of Technical Physics
(ITEP)

Reviewer:	Prof. Dr. Ron Dagan
Second reviewer:	Dr. Klaus-Peter Weiss
Advisor:	Dr. Nadja Bagrets
Second advisor:	Prof. Dr. Laura Savoldi

01. March 2024 – 22. October 2024

Karlsruher Institut für Technologie
76128 Karlsruhe

I declare that I have developed and written the enclosed thesis completely by myself, and have not used sources or means without declaration in the text.

PLACE, DATE

. . . . . .

(Simone Severo)

Abstract

High Temperature Superconductors (HTS) are promising candidates for high current Cable-In-Conduit Conductors (CICC) for large high-field magnets. In many cases, these CICCs are made from several HTS strands, which themselves consist of individual HTS tapes.
Quench propagation in CICCs is currently under intensive investigation, and it can be predicted by modelling the entire cable structure. To model the heat transfer, along with material properties the thermal properties of contact interfaces between structural materials are highly needed. There are different kinds of thermal contacts in CICC: contacts between superconducting tapes stacked together, contacts between thin copper of stainless steel tapes, and between bulks of structural materials.
This work focuses on characterizing the thermal contact resistance between metallic surfaces in various configurations relevant to high-current HTS CICC systems. Experiments were conducted across a range of pressures (50 N to 200 N) and temperatures (6 K to 300 K) to assess the thermal contact resistance behavior. The analysis included both soldered, unsoldered HTS tapes and the BRAST braid. For soldered tapes, surface treatments using citric acid were applied to reduce the presence of surface oxides, while unsoldered stacks and BRAST braid were evaluated under different pressure conditions to determine the impact on contact area and heat transfer.

The results of this study provide a comprehensive overview of thermal contact resistance behavior under varying operational conditions, contributing valuable insights into the design and thermal management of superconducting cables for fusion reactors and other high-current applications.

Contents

List of Figures

List of Tables

1 Fundamental Concepts: Superconductivity and Nuclear Fusion

1.1 Introduction

The landscape of high-temperature superconductors (HTS) is dealing with cutting-edge technologies, such as nuclear fusion. In the pursuit of controlled nuclear fusion, superconducting magnets play a pivotal role in confining and controlling the plasma within the reactor.
High-temperature superconductors offer a promising avenue for constructing these magnets due to their ability to operate at temperatures higher than traditional low-temperature superconductors.
As the fusion reactor operates at extreme temperatures and magnetic fields, any mismatches in thermal properties at the interfaces can lead to localized heating, compromising the structural integrity of superconducting components and impeding the fusion process's overall efficiency.
In order to have a better comprehension of this work, in this chapter a brief introduction to the peculiar properties of superconductors and their application in nuclear fusion are proposed.

1.2 Superconductivity

1.2.1 The Phenomenon of Superconductivity

The phenomenon of superconductivity, characterized by the complete absence of electrical resistance and the expulsion of magnetic flux below a so-called *critical temperature* (T_C), stands as one of the most intriguing and transformative discoveries in the realm of condensed matter physics.

In 1911, the physicist Heike Kamerlingh Onnes achieved a breakthrough in the quest to understand electrical conductivity at low temperatures.
Through experimentation involving the liquefaction of Helium, he observed as shown in figure 1.1 a sudden drop in the electrical resistance of mercury as it approached a critical temperature, of approximately $4.2K$ [1].

Several years later, in 1933, Meissner and Ochsenfeld found out the unique electromagnetic properties exhibited by some materials when cooled below a critical temperature to completely expel an external magnetic flux[2].

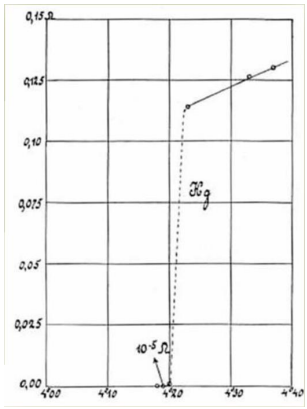

Figure 1.1: Plot of resistance versus temperature for Mercury, from [1].

This behavior is explained through the presence of screening currents flowing all over the surface of the superconductor. These currents produce a magnet field that is opposite and equal in intensity to the applied field, leading to the complete magnetic field expulsion, as shown in figure 1.2.

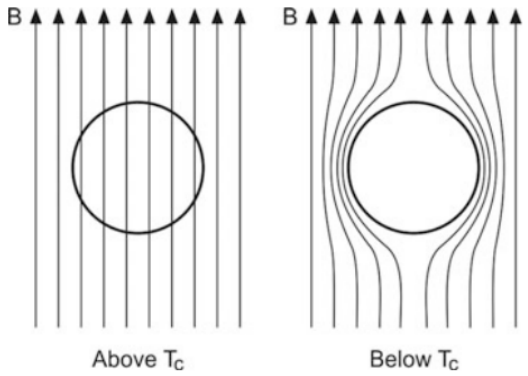

Figure 1.2: The Meissner Effect under and above the critical temperature, from [3].

1.2.2 Type-I and Type-II superconductors

When a superconductor is subjected to a magnetic field exceeding a certain critical threshold, its superconducting properties can be disrupted, causing a transition back to a normal, resistive state.
This led to the definition of a *critical magnetic field*, denoted as B_C, which represents the maximum intensity of the external *magnetic field* that a superconductor can tolerate before losing its superconducting properties.

Superconductors can be categorized into two types based on their response to an external magnetic fields: Type-I and Type-II [3].

Type-I superconductors, following the Meissner effect, expel almost all magnetic flux from their interior below the critical magnetic field.
Some examples of Type-I superconductors include elemental superconductors such as lead (Pb) and tin (Sn).

Type-II superconductors have a more complex response to magnetic fields, characterized by multiple critical fields, as shown in figure 1.3.

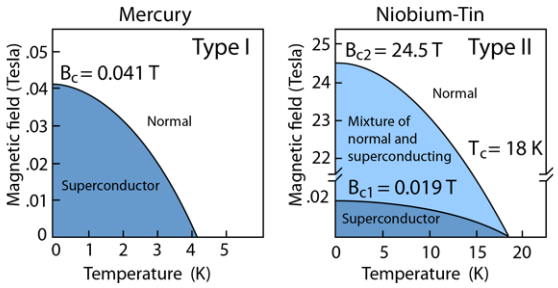

Figure 1.3: Magnetic phase diagrams of type-I (Mercury) and type-II (Niobium-Tin) superconductors, from [4].

Below the lower critical field, B_{C1}, type-II superconductors expel magnetic flux through the Meissner effect. Between the lower critical field and the upper critical field B_{C2}, type-II superconductors allow partial penetration of magnetic flux in the form of quantized vortices, within which the superconducting properties are lost, delineating small cores of normal conductivity, in the so-called vortex state, as shown in figure 1.4.
Examples of type-II superconductors are cuprates or niobium alloys.

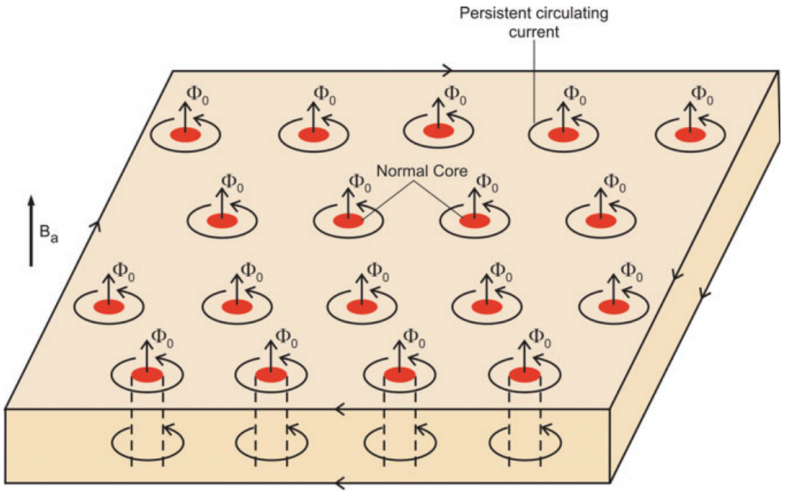

Figure 1.4: Quantized vortexes in the vortex state between B_{C1} and B_{C2}, from [3].

Each of the vortexes carries a unit quantum of flux $\Phi_0 = h/2e$ parallel to the applied field.
The diameter of the vortexes is an intrinsic property of the superconductor, the *coherence*

length ξ, proposed by V.L. Ginzburg and L.D. Landau in the Ginzburg-Landau Theory [5]. The magnetic vortexes penetrate the superconductor diminishing exponentially to negligible levels over a characteristic distance known as the *penetration depth* denoted by λ.
Ginzburg and Landau also introduced in their theory the GL-parameter, denoted by κ, which represents the ratio of the *penetration depth* to the *coherence length* in a superconductor.
From the value of the GL-parameter type I and type II superconductors can be distinguished:

- $\kappa < \frac{1}{\sqrt{2}}$ for type-I superconductors;
- $\kappa > \frac{1}{\sqrt{2}}$ for type-II superconductors.

Type-II superconductors are more technologically significant due to their ability to maintain superconductivity at higher magnetic fields, most superconductor applications are based on type-II superconductors.

1.2.3 High-temperature superconductivity

The phenomenon of superconductivity manifests at extremely low temperatures. In 1987 the first advancement in high-temperature superconductors was unveiled by Georg Bednorz and K. Alex Müller [6]. One year later, Ching-Wu Chu et al. [7] made the first high-temperature superconductor with a critical temperature of 93 K, a Y-Ba-Cu-O compound system.
It is feasible to categorize superconducting materials based on their critical temperatures:

- Low-temperature superconductors (LTS);
- High-temperature superconductors (HTS).

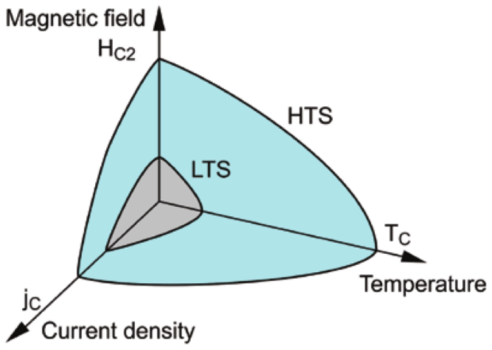

Figure 1.5: Comparison between HTS and LTS critical surfaces, from [8].

In 1916 Francis Silsbee [9] proposed the *critical current*, J_C, which refers to the maximum current density that can flow through the material before it transitions from its superconducting state to a resistive state.
The *critical current*, coupled with the *critical magnetic field* and the *critical temperature*,

led to define the critical surface of a superconductor, which is usefull to evaluate the performance of superconductors. As shown in figure 1.5, HTS are characterized by higher critical parameters, enabling their use in a wider range of applications.
In table 1.1 critical parameters of different superconductors are shown.

Table 1.1: Critical parameters in different superconductors, from [10]

Material	$T_C[K]$	$B_C[T]$	$J_C[A/cm^2]$
$NbTi$	9.2	14.5	$4x10^5$
Nb_3Sn	18	28	$\sim 10^6$
MgB_2	39	18	$\sim 10^6$
$YBCO$	93	> 100	$\sim 10^7$
$Bi-2201$	33	> 100	$\sim 10^6$
$Bi-2212$	96	> 100	$\sim 10^6$
$Bi-2223$	104	> 100	$\sim 10^6$

As scientific inquiry into superconductors advances over the years, various classes of HTS materials have been discovered:

- Cuprates, layered crystal structure with of copper–oxygen planes [11];
- Iron-based, with layers of iron and a pnictogen or a chalcogen [12];
- Carbon-based [13];
- Magnesium diboride, with a layered hexagonal structure [14];
- Nickelates, analogs to cuprates [15].

In most cases, these material classes exhibit a stratified structure, as shown in figure 1.6, in which the superconducting current manifests across the layers.

Cuprates

Cuprates are layered materials, as shown in figure 1.6, with superconducting layers of copper oxide, separated by layers containing ions such as lanthanum, barium, strontium, or other atoms in order to stabilize the structures and act as dopant for current carriers in the copper-oxide layers. This peculiar layered structure led to a high anisotropy in normal and superconductive properties, with a higher conductivity parallel to the copper-oxide layer than the perpendicular direction [17]. The copper-oxide planes are based on a checkerboard lattices with O^{2-} ions at the squares and Cu^{2+} ions at the center of each square. Critical temperatures of this class of materials are related to the presence of adjacent ions, chemical composition, and oxygen content.
The most used materials are Yttrium barium copper oxide and Bismuth strontium calcium copper oxide.

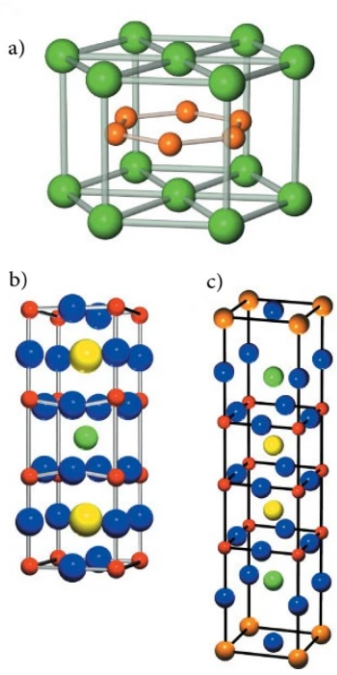

Figure 1.6: Different HTS layered structures: a)Magnesium diboride (MgB_2), b)Yttrium barium copper oxide ($YBCO$), c)Bismuth strontium calcium copper oxide ($Bi-2223$), from [16].

YBCO

The yttrium barium copper oxide, also known as *YBCO* is a group of crystalline chemical compounds, which is part of a more general group of rare-earth barium copper oxides (*ReBCO*). The general formula for this family of compounds is $YBa_2Cu_3O_{7-x}$ and the most used in superconductive technology is the $YBa_2Cu_3O_7$ of which the structure is shown in figure 1.6. Among the cuprates group, *YBCO* is the least anisotropic and the critical temperature for this material is 93 K [3].
A granular structure characterizes this material and the grain boundaries are weakly conducting, nevertheless, high critical current densities have been demonstrated [18]. Inside the grains, the critical current density is about 10^6 Acm^{-2} at 77 K [3].

BSCCO

Bismuth strontium calcium copper oxide (*BSCCO*) is part of the cuprates family and is the first discovered high-temperature superconductive material without the presence of a rare-earth element [19]. The general chemical formula for this material is $Bi_2Sr_2Ca_{n-1}Cu_nO_{2n}$, from the value of n, there are:

- $n = 0$, $Bi-2201$;
- $n = 1$, $Bi-2212$;
- $n = 2$, $Bi-2223$.

Table 1.2: Critical temperature in different Bi-cuprates

Compound	$Cu-O$ layers	T_C [K]
$Bi-2201$	1	33
$Bi-2212$	2	96
$Bi-2223$	3	104

As shown in figure 1.7, the structure is based on $Cu-O$ layers separated by $Sr-O$ and $Ca-O$ layers and two double $Bi-O$ layers at the ends of the unit cell.

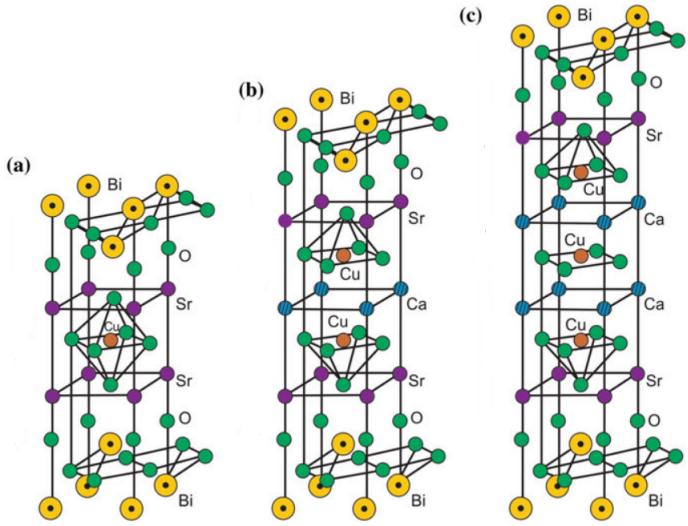

Figure 1.7: Different $Bi-cuprate$ structures: a)$Bi-2201$, b)$Bi-2212$, c)$Bi-2223$, from [3].

The critical temperature is strictly related to the number of $Cu-O$ layers, as shown in 1.2, T_C increases with the number of $Cu-O$ layers until three layers are reached, and then it decreases.

1.3 Nuclear fusion

1.3.1 Nuclear fusion power

Nuclear fusion power currently stands as a method of power generation in the research and development phase, aimed to produce electricity from the nuclear fusion reaction between two light nuclei.
A nuclear fusion reaction involves two or more atomic nuclei, which produce heavier nuclei releasing a huge amount of energy. The most common fusion reaction, the so-called $D-T$ reaction, as shown in figure 1.8, involves two hydrogen isotopes, deuterium and tritium, which under conditions of high pressure and high temperature where the electrostatic repulsion between the nuclei is overcomed, fuse producing a heavier nucleus

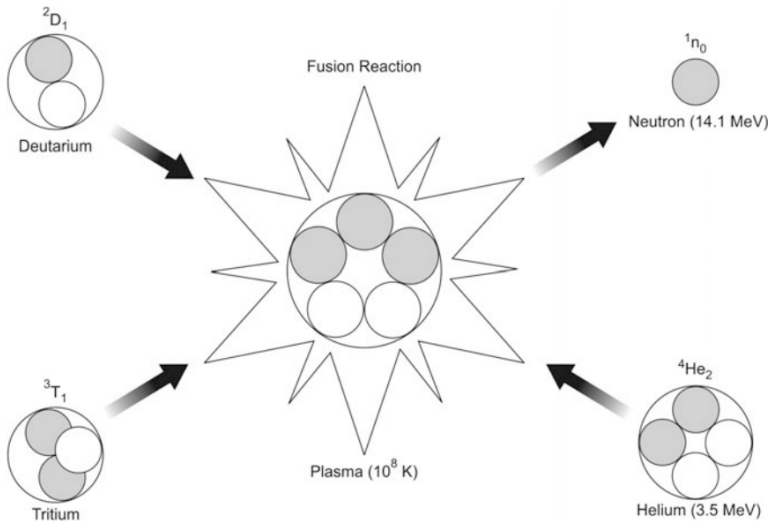

Figure 1.8: Fusion Reaction between deuterium and tritium, from [3].

of helium and release a huge amount of energy, through a 14.1MeV energetic neutron [3]. Fusion reactions occur in the sun and stars, which are characterized by high pressure due to a high gravitational pull and very high temperatures [20]. To achieve these extreme conditions of temperature and pressure is necessary the transformation of matter into a high-energy state known as plasma.
Plasma is one of four fundamental states of matter based on a gaseous mixture of positive ions and electrons. Plasma can be fully or partially ionized, in function of its temperature, density and presence of neutral particles [21]. To create the massive gravitational pull the idea is to raise the temperature of the plasma to $\sim 10^8 K$, moreover, the plasma has to remain dense enough in order to let the fusion reactions continue and reach *ignition* condition, in which the heating of the plasma by the helium nuclei is equal to the heat loss. In 1957, the Lawson's criterion was proposed as a condition for reaching the plasma self-sustaining [22]:

$$n_e T \tau_E > \frac{12 k_B T^2}{E_{ch} \langle \sigma v \rangle} \tag{1.1}$$

where:

- n_e is the plasma density;
- τ_E is the energy confinement time;
- T is the plasma temperature;
- k_B is the Boltzmann constant;
- E_{ch} is the energy of the charged fusion product;
- $\langle \sigma v \rangle$ the average of Maxwellian velocity distribution at temperature T.

The energy confinement time, τ_E, is given by the ratio between the energy density and the power loss density:

$$\tau_E = \frac{W}{P_{loss}} \tag{1.2}$$

The $D - T$ reaction releases a fast-moving neutron. Neutrons being electrically neutral are unaffected by the confinement of plasma. The neutron gets captured in a blanket containing a working fluid which gets heated up and used to produce steam for rotating turbines, with the aim of producing electricity as a conventional power plant, as shown in figure 1.9.

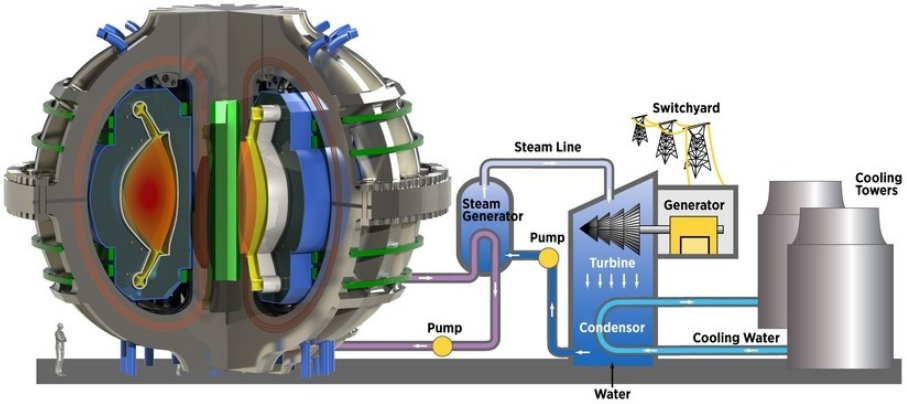

Figure 1.9: Electrical power generation using a fusion reactor, from [23].

1.3.2 Plasma confinement

In nuclear fusion research, one of the leading challenges lies in plasma confinement, which refers to the restriction of plasma by different kinds of forces at the extreme conditions needed for thermonuclear fusion reactions.
Two are the methodologies employed for plasma confinement, inertial confinement and magnetic confinement.

Inertial confinement

Inertial confinement fusion (ICF) is an approach to achieve controlled nuclear fusion reactions. The fundamental principle involves utilizing laser or particle beams to compress and heat a target containing fusion fuel, a $D - T$ mixture, in order to satisfy the Lawson criterion and reaching the ignition conditions.

Magnetic confinement

Magnetic confinement fusion (MCF) is a plasma confinement technique based on the use of high magnetic fields. Magnetic confinement relies on the concept that the electrically charged particles within the plasma move in a spiral pattern aligned with the magnetic

field direction, as shown in figure 1.10. With the development of scientific research in the field of nuclear fusion, there are three main methods of magnetic confinement: Magnetic mirror, Stellarators and Tokamak. Among these, stellarators and tokamaks are

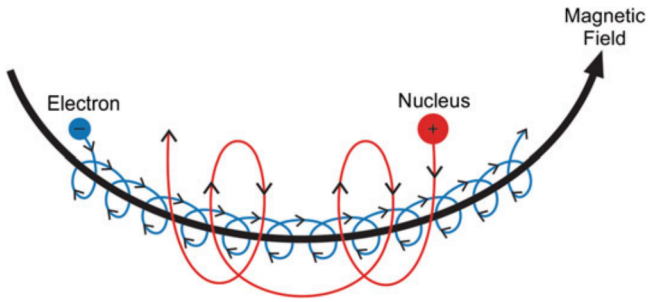

Figure 1.10: Charged particles paths around the magnetic field, from [3].

of particular scientific interest due to their potential for sustained plasma confinement and their extensive development in fusion research.

The Stellarators

The Stellarator concept was introduced by Lyman Spitzer, in *Project Matterhorn* at Princeton University during 1951. The technique proposed by Spitzer is based on preventing plasma escapement by solenoidal coils bent into a torus, closed at the two ends. A rotational transform characterizes the design involved in the Stellarator, the system is arranged such that a magnetic field line passing through it intersects a cross-sectional plane, with the points of intersection then revolving around the magnetic axis [24]. This leads to a complex scheme of magnetic coils, convoluted to have the desired plasma shape, as shown in figure 1.11.

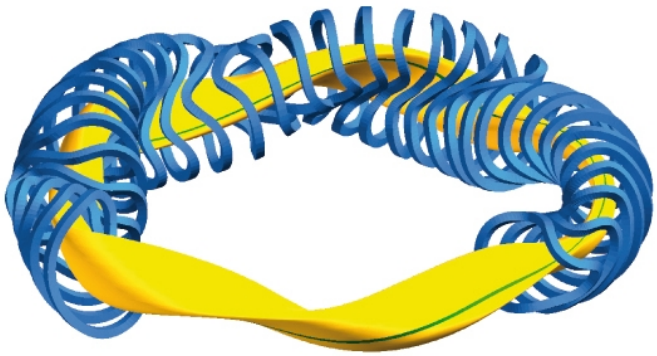

Figure 1.11: Exemple of Stellarator design: magnet coils (blue) and the plasma (yellow). A magnetic field line is highlighted in green on the yellow plasma surface, from [25].

This complex configuration eliminates the need for an internal current inside the plasma,

allowing a steady state operation after the ignition achievement, removing a large class of instabilities.

The Tokamak

In 1950, was proposed by Oleg A. Lavrent'ev the idea to develop a system with electrostatic confinement of hot plasma to realize thermonuclear fusion.
One year later, Andrej D. Sakharov and Igor E. Tamm came up with the idea of confining plasma in a toroidal chamber using a strong longitudinal magnetic field. They thought to counterbalance the toroidal drift of charged particles through a poidal magnetic field induced by the plasma itself [26]. The proposed device was called Tokamak, a Russian acronym meaning *TOroidal CHAmber with MAgnetic Coils*.
The plasma confinement inside the Tokamak is achieved through the combination of two magnetic fields, resulting in a helical field, as shown in figure 1.12:

- poloidal field, produced by the current circulation inside the plasma, induced by the central solenoid (inner poloidal magnetic field coil) ,acting as a primary of a transformer (in alternate current regime) and the plasma as the secondary, and the outer poloidal magnetic field coils;
- toroidal field, produced by the toroidal coils around the torus.

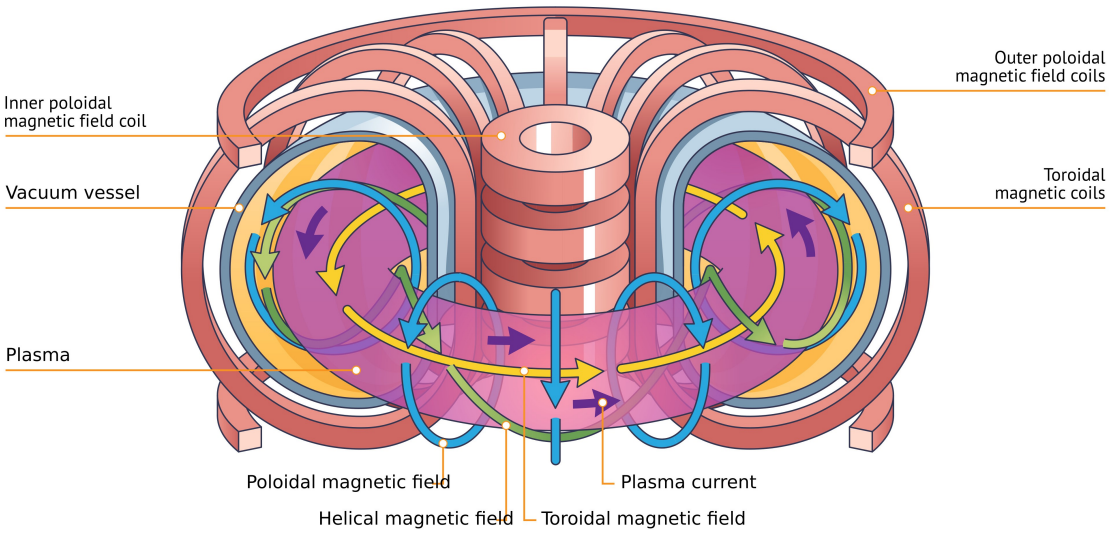

Figure 1.12: Magnetic fields in tokamak: toroidal magnetic field (yellow), poloidal magnetic field (light-blue) and helical magnetic field (green), from [25].

2 Superconductive cables

Superconducting cables play a crucial role in nuclear fusion reactors due to their ability to generate extremely strong magnetic fields. In fusion devices, such as tokamaks or stellarators, magnetic fields are essential to confine and control the plasma. Traditional electromagnets, made of resistive materials, suffer from significant energy losses due to resistive heating, especially when generating the intense magnetic fields required for plasma confinement. For this reason, over the years, research has led to the development of superconducting cables, which are examined in detail in this section.

2.1 LTS and HTS cables

Nowadays, one of the most important superconductors application refers to power cable, due to the capabilities of superconductive materials to carry high current densities. Both HTS and LTS cables adopt the Cable-In-Conduit Conductors concept, also known as CICC, firstly proposed in 1975 [27]. Different cable concepts have been developed over the years, allowing the distinction between two generations of cables:

- *LTS cable*, consist of a certain number of superconducting filaments embedded in a conductive material matrix, forming strands transposed and twisted together in a rope-like pattern and inserted into a jacket with a central cooling channel, as shown in figure 2.1. The superconductive materials in most of the cables based on this configuration are $NbTi$ (LTS), Nb_3Sn (LTS) and MgB_2 (HTS).

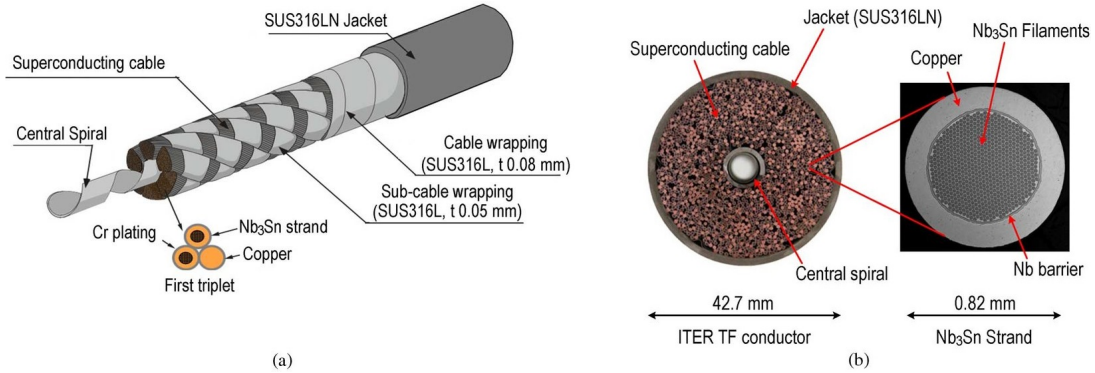

Figure 2.1: Diagram and photographs of a typical LTS cable. (a) Schematic diagram of the CICC. (b) Cross sections of the CICC and superconductive filament embedded in a copper matrix, from [28].

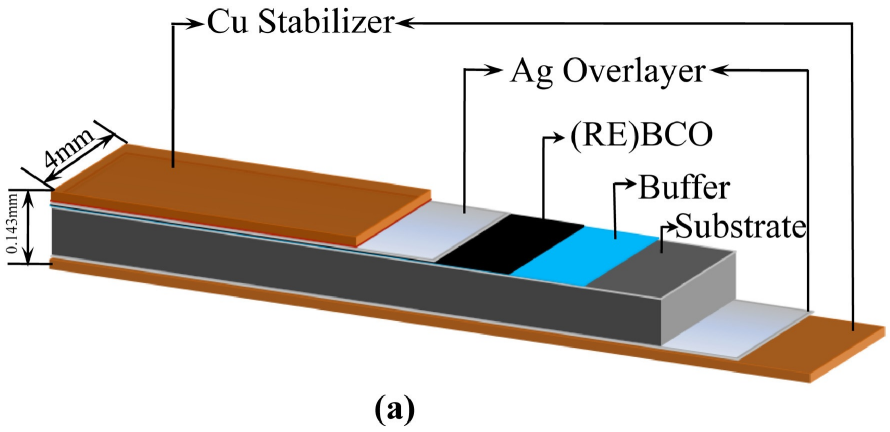

Figure 2.2: Architecture of the HTS tape conductor, from [29].

- *HTS cable*, the design, shown in figure 2.2, is based on a multi-layered structure characterized by a mechanical substrate on which a buffer, a superconductive film and a silver layer are deposited and coated with a stabilizer. The superconductive material in most of the cases is *REBCO*.

In this configuration of cable, each layer provides a different improvement [30][31]:

- *REBCO layer*: responsible for the flow of electric current during steady-state operation;
- *Silver over-layer*: connected in parallel with the HTS layer to provide thermal stability and to protect the cable from thermal-induced damage, for compatibility issues with the *REBCO* layer copper is avoided;
- *Buffer layer*: based on a triple structure; a barrier layer which blocks atomic diffusion, a template layer with a textured surface for the deposition of the superconductive material, and a seed layer needed to help the crystallization of the materials over the metal substrate;
- *Substrate*: giving mechanical strength to the tape, made of flexible Ni or $Ni-based$ alloys such as $Hastelloy$;
- *Stabilizer*: usually made of copper in order to provide thermal stability, as the silver over-layer.

2.2 HTS cable configurations

In this section, different configurations and development of HTS are presented.

2.2.1 Al-slotted core cable

In 2014, ENEA with the industrial partner TRATOS-cavi designed and prototyped a helical twisted-stacking tape cable (TSTC), applicable for both high-field magnet conductor and power transmission or distribution purposes [32].

Cable design

The layout, as shown in figure 2.3, is based on a central and twisted aluminum core, with a diameter of 19 mm, provided with five slots, each measuring 4.3 mm × 4.3 mm, designed to house stacks of 4-mm wide HTS tapes. There are 150 HTS tapes, bundled in 5 stacks, resulting in 30 tapes per stack [32]. The cable is surrounded by an external aluminum or

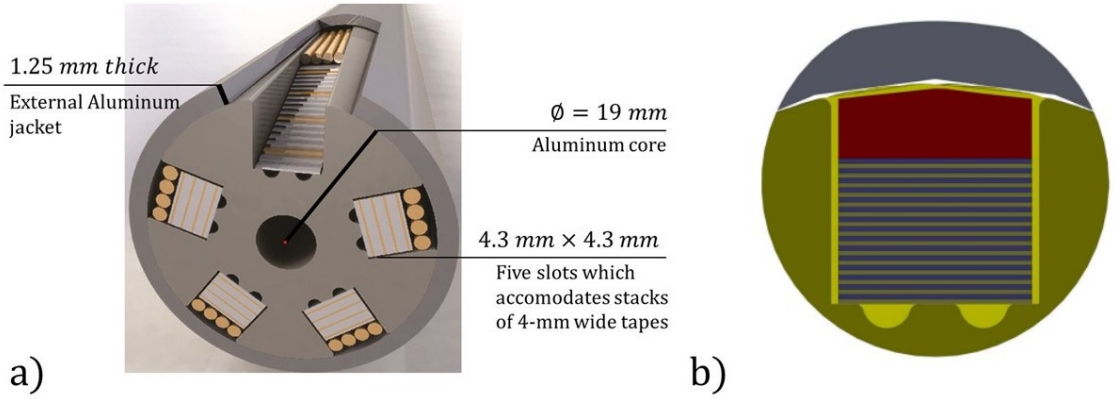

Figure 2.3: (a) Artistic view of the Al-slotted core cable designed by ENEA, with dimensions, from [33]. (b) Cross-sectional view of a slot with 30 HTS tapes, the spacer and the secondary sub-channels , from [32].

steel structural jacket, with a thickness equal to 1.25 mm, to provide mechanical strength. In the upper part of the stack, towards the outer periphery, there are copper or aluminum spacers, ensuring a suitable connection with the aluminum casing. The main central channel, with a 4 mm diameter, paired with the secondary sub-channels around the stacks provide a good coolant flow rate [33]. During the years, as shown in figure 2.4, different prototypes of this cable were developed, tested and modified, from five to six slots [34].

2.2.2 CroCo cable

In 2016, based on the TSTC architectures, Karlsruhe Institute of Technology (KIT) proposed the HTS CrossConductor cable, also known as HTS CroCo cable [35]. The CroCo cable is based on strand built up on a long-length, twisted and soldered tape assembly, embedded in a continue copper tube.

Cable design

The individual strand design aims to maximize current density by employing rectangular-shaped HTS tapes, allowing a cross-section suitable for twisting. The compromise between

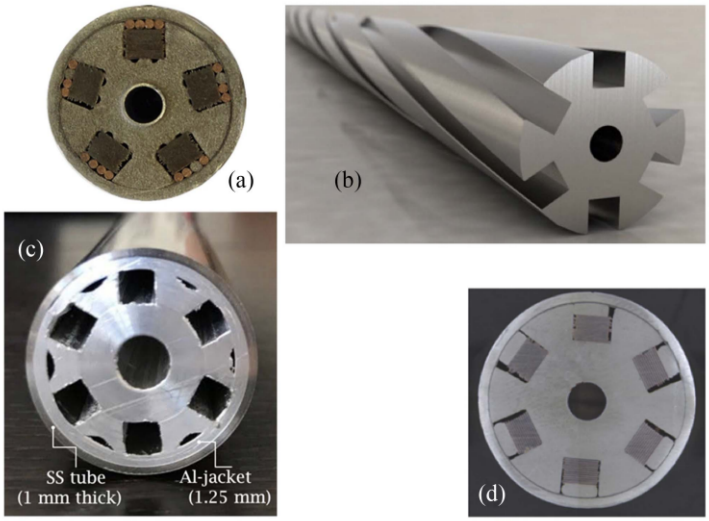

Figure 2.4: Different ENEA-TRATOS Al-slotted cable prototypes: (a) 5-slots sample; (b) rendering of a 5-slots sample; (c) different 6-slots sample with improved cooling capacity; (d) 6-slots sample, from [34].

the two requirements is obtained using parallel tapes of different widths, as the one shown in figure 2.5, characterized by tapes with widths of 4 mm and 6 mm.

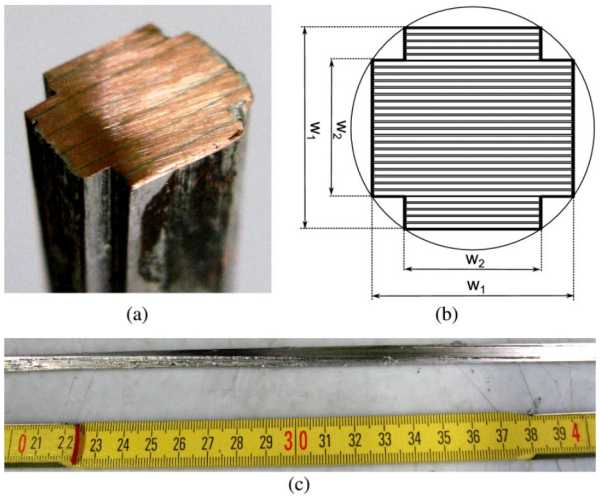

Figure 2.5: Single strand CroCo cable design: (a) cross-section, (b) schematics, (c) top images of a twisted Croco strand with twist pitch of 80 cm, from [35].

Stacking, twisting and soldering processes are done in different fabrication steps, in order to avoid formation of oxides, voids or contaminations on the tapes. The twisting process occurs while the solder around the tape stacks is still liquid, at high temperatures (more than 230^oC for $Pb37Sn63$ solder).
The single strand is then encapsulated in a copper tube, as shown in figure 2.6, in order to enhance the cross-section available in the event of a quench, and to strengthen the strand against Lorentz forces [35].

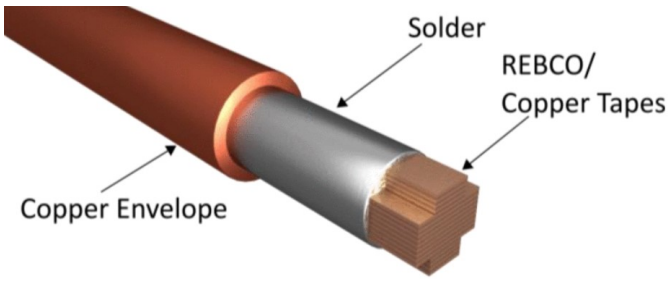

Figure 2.6: Single strand with copper envelope, from [36].

KIT proposed and tested three final cables options [37], as shown in figure 2.7:

a) 3 CroCo strands embedded in a copper sheath of 2 mm thickness;

b) 3 CroCo strands embedded in a copper sheath of 2 mm thickness;

c) 3 CroCo strands embedded in copper profiles for larger contact areas.

The final assemblies are both based on the presence of three CroCo strands embedded in a stainless steel jacket paired with different cooling channels, with a forced flow of supercritical Helium.

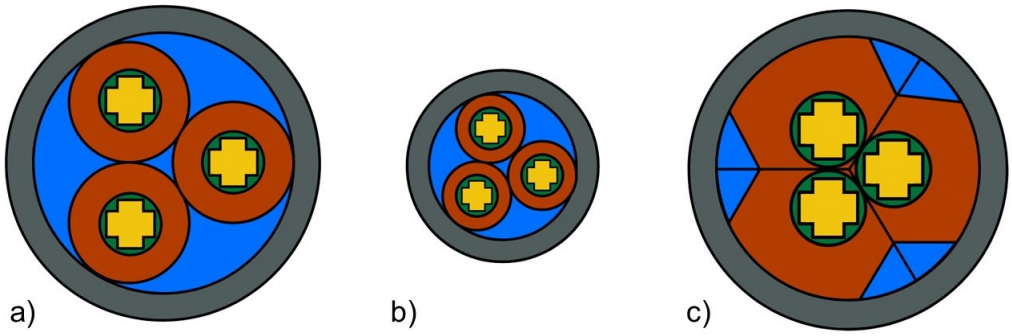

Figure 2.7: Layout of three conductor options: a) CroCo strands with a copper sheath of 2 mm thickness, b) CroCo strands with a copper sheath of 1 mm, c) CroCo strands embedded in copper profiles for larger contact areas. Each color represent a different material: HTS strand in yellow, copper jacket in brown, solder in green and helium channels in blue, from [37].

The geometric parameters of the various CroCo cables options are illustrated in table 2.1.

Table 2.1: Geometric parameters in different CroCo cables options, from [37]

Parameter	Unit	option a	option b	option b
Diameter of CroCo	mm	8	6	4.2
Inner diameter of stainless steel jacket	mm	17.24	12.93	15.00
Jacket thickness	mm	1	1	1
Hastelloy cross section inside HTS tapes	mm^2	9.60	9.60	9.60
REBCO cross section inside HTS tapes	mm^2	0.192	0.192	0.192
Copper cross section inside HTS tapes	mm^2	13.44	13.44	13.44
Silver cross section inside HTS tapes	mm^2	0.729	0.729	0.729
Solder cross section inside HTS tapes	mm^2	13.7	13.7	19.72
Additional copper cross section	mm^2	113.097	47.124	107.24
Cooling channel cross section	mm^2	82.57	46.45	25.78
Jacket cross section	mm^2	57.30	43.76	50.27

2.2.3 VIPER cable

In 2020, the VIPER (which stands for Vacuum Pressure Impregnated, Insulated, Partially transposed, Extruded, and Roll-formed) was developed by Commonwealth Fusion Systems in collaboration with MIT-Plasma Science and Fusion Center in order to improve the Al-slotted core cable proposed by ENEA, analysed in the previous section 2.2.1.
This cable, related to the previous configuration, presents: a simplified configuration based on the TSTC concept, a higher current density and a vacuum pressure impregnation (VPI) solder process, to connects the HTS tapes within the cable and the other regions to the copper former [38].

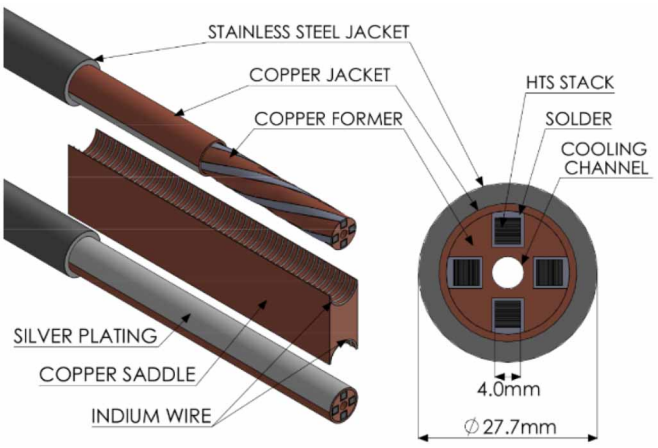

Figure 2.8: VIPER cable design: (Left) the cable structure and (Right) the cable cross section, from [38].

Cable design

The cable design, shown in figure 2.8, is based on the presence of a central leak-tight channel in which flows cryogenic coolant, surrounded by a copper core with extruded rectangular channels supporting HTS stacks. The extrusion and HTS stacks are twisted to prevent the build-up of stresses in HTS during its production, especially when is shaped into a coil, and to decrease transient heat generation related to changing magnetic fields which disrupt the flow of magnetic flux within the HTS layers [38].
The VPI solder process couple the HTS tapes to the other regions in different ways [38]:

- mechanically: soldering transforms the cable into a solid, unified structures where internal components remain fixed with no movement, preventing mechanical degradation related to electromagnetic loading and cycling;
- electrically: it guarantees efficient flow of electricity between each HTS tape in a stack and between the HTS stacks themselves and the copper former, resulting in a low-resistance current and a uniform current distribution;
- thermally: soldering establishes a route for heat produced or accumulated within the HTS stack to transfer effectively through the copper former to the central coolant channel.

2.2.4 SECAS cable based on BRAST

In 2023, starting from the Al-slotted cable previously developed (analysed in section 2.2.1), ENEA proposed a new HTS sector-cable concept [34]. ENEA developed a cable based on a multi-stage configuration, combination of sub-cables, formed with different sub-units.

Cable design

The design proposed by ENEA the SECtor ASsembled Cable, SECAS, is based on the sub-unit of BRAided STack of tapes, also called BRAST.
The BRAST sub-unit, shown in figure 2.9, presents a certain number of HTS tapes is incorporated within a braid of thin, tin coated copper wires, with different diameters from 0.1 mm to 0.3 mm. In accordance with the required usage, various sub-unit proposals have been examined, featuring tapes 4 mm and 12 mm in width [34]. From the BRAST sub-unit, the sub-cable unit is obtained using an extruded sector-shaped profile, where one or more BRAST should be inserted, and sealed with a filler and an outer covering made of either copper or steel tape with an open mesh, as shown in figure 2.10.
In the final assembly, shown in figure 2.11, the sub-cables are installed around a central cooling spiral, wrapped with an outer open mesh steel tape and then a final layer of steel as external jacket [34]. The central cooling spiral let the cooling fluid to distribute around the gaps within the sub-cables.

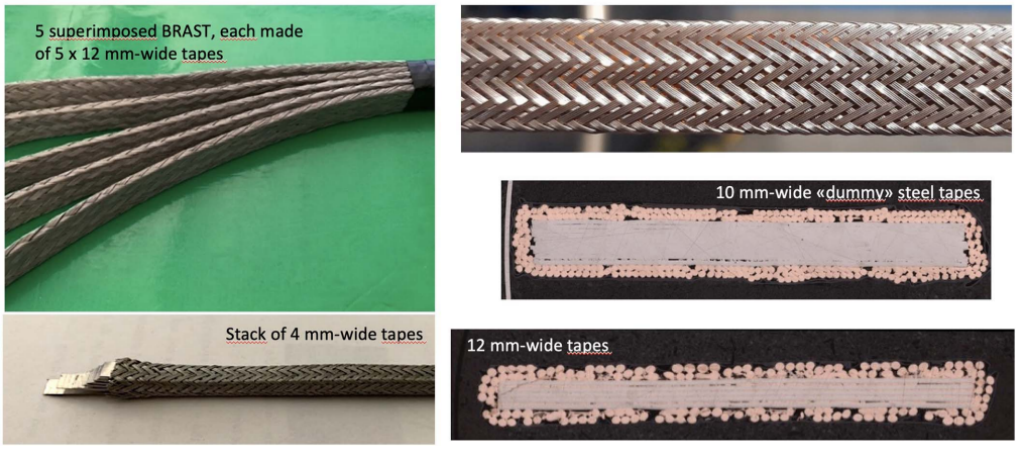

Figure 2.9: Different BRAST prototypes, from [34].

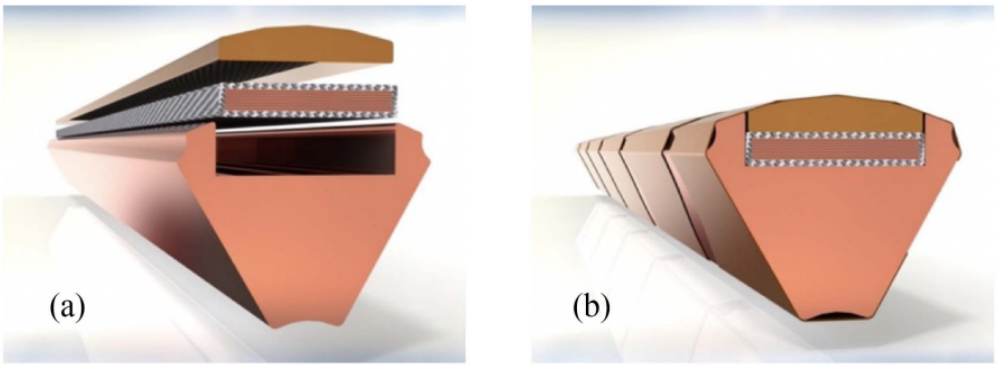

Figure 2.10: Render of the sub-cable: (a) the extruded sector shaped core and BRAST sub-unit, (b) closed sub-cable with a filler and an outer wrapping, from [34].

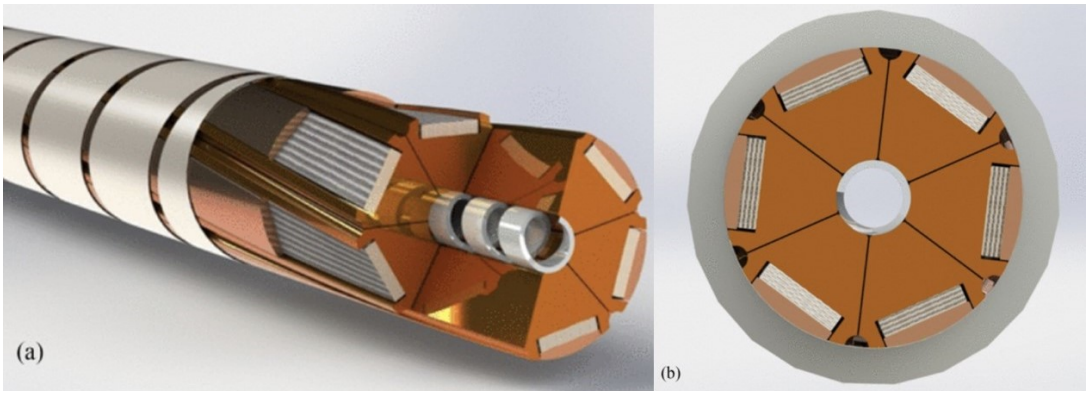

Figure 2.11: Assembled SECAS cable: (a) with BRASTs, sector shaped core, fillers, outer steel wrap, and central spiral; (b) schematic representation of the cross-section, with the external steel jacket, from [34].

2.3 Quench in superconductors

In superconductive materials, quench is a term which refers to the anomalous transition from superconducting behavior to resistive one, during the operation, as shown in figure 2.12.

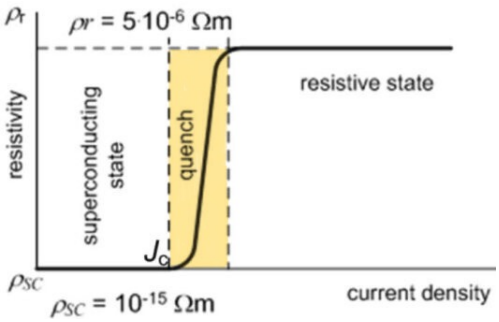

Figure 2.12: Superconductors resistivity related to current density during quench, from [39].

This transition occurs when one of the parameters characterizing the superconductor, such as current, magnetic field, or current density, exceeds its critical value. The Joule heating (I^2R) across the resistive segment will propagate rapidly throughout material, causing the magnet to lose its superconducting state and to release the stored energy ($\frac{1}{2}LI^2$). This thermal energy leads to the raising of the magnet's temperature, and consequently, the propagation along and across the length occurs. The propagation of quench, in LTS and HTS, manifests in distinct manner. As shown in figure 2.13, the quench propagation's timescales are really different.

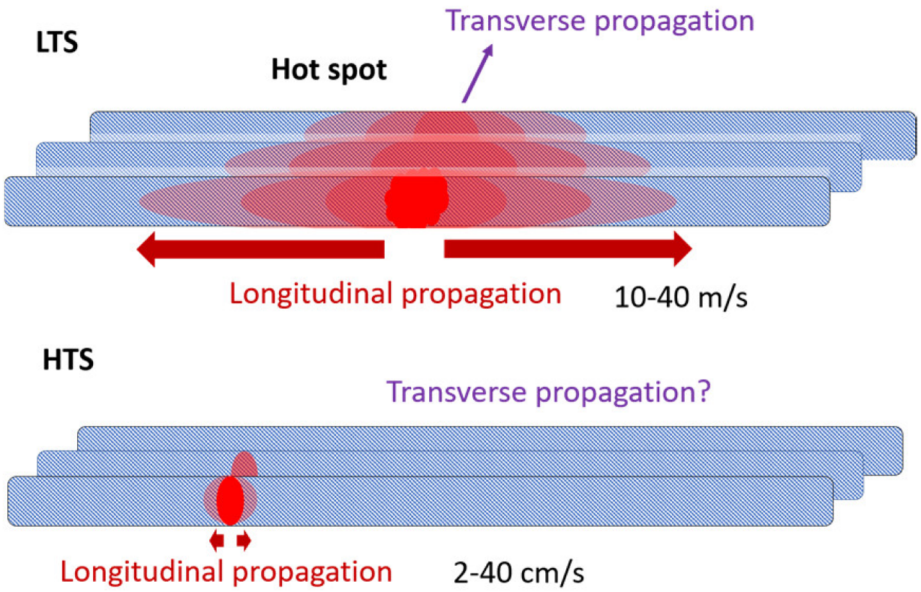

Figure 2.13: Quench propagation comparison in HTS and LTS, from [40].

Comparing in term of quench protection an HTS to a LTS cables, this behavior is due to different motivations [41]:

- the specific heat varies directly with the cube of the temperature, a HTS operating at 40 K exhibits a specific heat approximately 700 times greater than a LTS at 4.5 K, resulting in a quench velocity roughly 60 times lower at the same current density;
- HTS are based on a lower amount of copper, this lead to a lower avarage thermal conductivity of HTS conductors and a thermal diffusivity of HTS typically two to three orders of magnitude lower than that of a LTS.

Quench can happen for several reasons, related to different parts in the magnet system [42]:

- Internal to the magnet, due to design errors, transients, leaks in cooling pipes and in vacuum parts;
- Failing or not appropriately designed magnet services, such as control system failures, false triggering of quench detection systems;
- External to the magnet, like radiation exposure, damages to cryo-lines or vacuum lines, sensors, valves.

Modeling the heat transfer in an entire cable structure can be a proper way to achieve a deeper comprehension regarding the propagation of quench in different configurations of HTS CICC. In order to model the heat transfer, particularly at the cryogenic temperatures at which superconductors operate, the thermal properties of contact interfaces between different materials play a fundamental role.

2.4 Relevant contacts in HTS cables

In the various proposed cable configurations, different types of contacts must be analyzed to accurately simulate the quench phenomenon. Contacts in superconducting cables involve diverse material types, including superconducting-superconducting material, copper-copper, copper-aluminum, and copper-stainless steel interfaces. In this section the various types of contacts analyzed will be examinated.

2.4.1 Soldered tapes

The VIPER cable, analyzed in the previous section 2.2.3, features HTS tapes soldered together. The contact between these soldered tapes will be one of the focus of the analysis. The type of contact studied can be viewed in the figure 2.14.

2.4.2 Unsoldered tapes and BRAST braid

In section 2.2.4, the SECAS cable, characterized by the inclusion of BRAST sub-units, was analyzed. Two thermal contact resistances were examined for this cable type: one between the braid and the tape, in figure 2.15 the red contact in the blue box, and the other between the tapes themselves, in figure 2.15 the red contact in the yellow box.

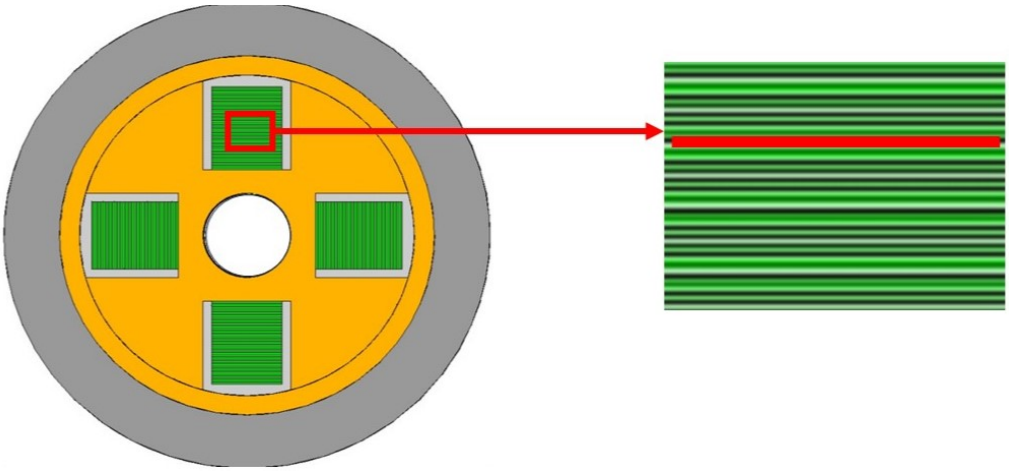

Figure 2.14: CAD of the VIPER cable, with a focus on the analyses contact (in red) between soldered tapes, from [43].

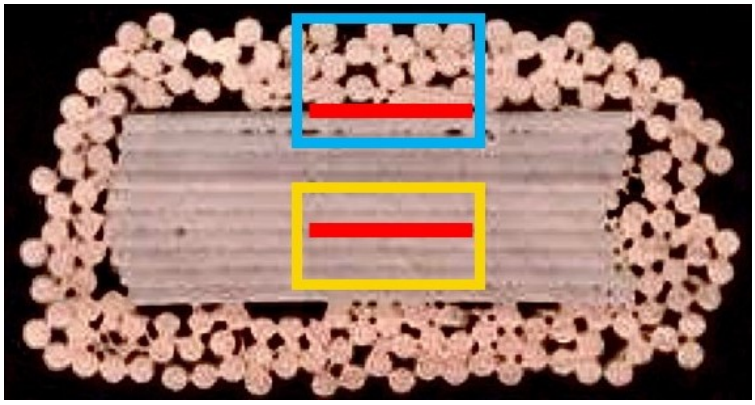

Figure 2.15: BRAST sub-unit section, with a focus on the analysed contacts in red: the yellow stays for the unsoldered tapes contact and the blue for the BRAID contact, from [44].

3 Thermal Contact Resistance

In systems where heat transmission occurs between two solid surfaces in contact, thermal contact resistance is an essential factor in thermal management. The resistance to the heat flow would be minimal if the two surfaces could be brought into perfect contact, devoid of contaminants, and without any gaps at the interface. Nevertheless, these conditions are ideal and not applicable in realistic contexts. The thermal contact resistance is defined as the ratio between the temperature drop across the interface and the heat flux between the bounding surfaces of the contact, measured in $\frac{K}{W}$ and expressed by the following equation:

$$R_{TC} = \frac{\Delta T}{\dot{q}} \tag{3.1}$$

In this work, the *thermal contact resistance* will be referenced by normalizing it with respect to the apparent contact surface area A_C, obtaining:

$$R_{TC} = \frac{\Delta T \cdot A_C}{\dot{q}} \tag{3.2}$$

measured in $\frac{K \cdot cm^2}{W}$.

3.1 Factors affecting thermal contact resistance

Several factors influence thermal contact resistance, from a macroscopic point of view [45]:

- surface roughness and waviness;
- thermal and mechanical properties of the materials;
- contact pressure;
- presence or absence of interstitial fluid;
- mean interface temperature.

This resistance arises from the incomplete contact between the interfacing surfaces. When two surfaces are pressed together, actual contact occurs only at a few discrete points due to the surface roughness and microscopic asperities of each surface. This lead the heat flux lines to converge to the solid-to-solid contact points, as shown in figure 3.1, which offer less resistance than the gaps. When the pressure on the contact is increased, the peaks in contact will deform, leading to an increase in both the size and number of contact

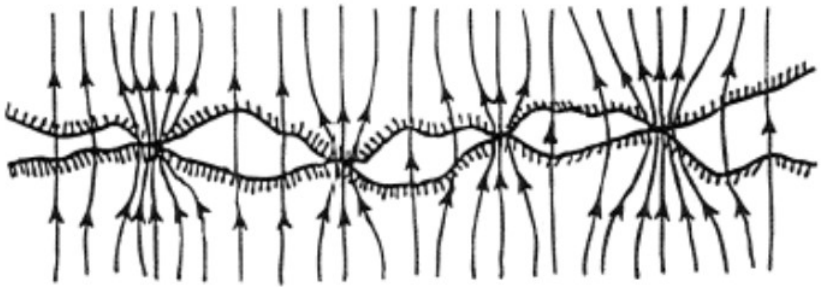

Figure 3.1: View of two materials in contact, with a magnified example of the heat flux lines convergence due to surface roughness and waviness, from [46].

points, thereby decreasing the thermal contact resistance. The presence of a fluid or solid interstitial medium between the contacting surfaces can either enhance or impede heat transfer at the junction, depending on the thermal conductivity, thickness, and hardness (in the case of a solid) of the interstitial medium. In vacuum, the primary mode of heat transfer is conduction conduction through the contact spots, resulting in an enhancement of the resistance [46].

3.2 Analytical expression for thermal contact resistance

Due to the significant number of parameters influencing contact resistance, it has not been possible to develop a single analytical expression for predicting contact resistance at the junction between two materials, except in cases of highly idealized single and multiple contacts. In the literature, the research concerning an analytical formulation of thermal contact resistance has been frequently addressed.
In 2019, Dhuley presented a comprehensive summary that compiles studies conducted over the past fifty years of research [47]. The proposed analytical formulation 3.3 for the total thermal contact resistance of a joint made of the same material at cryogenics temperature is:

$$R_{TC} = \frac{1}{A}\left(\frac{\sigma_s}{m_s}\right)\frac{1}{k_s}\left(\frac{p_{app}}{H_c}\right)^{-B} + \frac{16E_F}{\pi^2 k_B^2 n_e v_F}T^{-1}\left(\frac{p_{app}}{H_c}\right)^{-1} \tag{3.3}$$

The equation 3.3 is given by the addition in series of two different contributions to thermal contact resistance: *thermal constriction resistance* and *thermal boundary resistance*.

3.2.1 Thermal constriction resistance: applied force dependence

Thermal constriction resistance is predominantly governed by the microscopic contact between rough surfaces, where heat flow is constricted through micro-asperity contacts. As the applied force on these contacts increases, the asperities deform, resulting in an enlarged actual contact area. This deformation reduces the constriction resistance by providing more pathways for heat to flow, thereby enhancing thermal conductance. The thermal constriction resistance problem take into account three different component:

Table 3.1: Parameters and validity ranges for different thermal contact resistance models, from [47].

Model	A	B	Validity
Cooper, Mikic, Yovanovich	1.45	0.985	$3.6 \times 10^{-4} < p_{app}/H_c < 1.0 \times 10^{-2}$
Yovanovich	1.25	0.95	$10^{-6} < p_{app}/H_c < \times 10^{-2}$
Tien	0.55	0.85	-
Wheeler according to Mikic	1.13	0.94	-
Mikic and Rohsenow	0.90	0.941	-

- geometrical, to describe microscopically the contact between the surfaces;
- mechanical, to describe how the contact is affected by the surface hardness, the material elastic modulus, and the applied pressure;
- thermal, solving the heat diffusion equation through the contact.

The contact mechanics of two pressed solids, which make physical contact in a complex manner, are defined by the surface roughness parameter, σ_s, and the average slope of asperities, m_s, of each surface. The parameters are shown in figure 3.2 to provide a clearer understanding. Then, in order to take into account the thermal and mechanical properties,

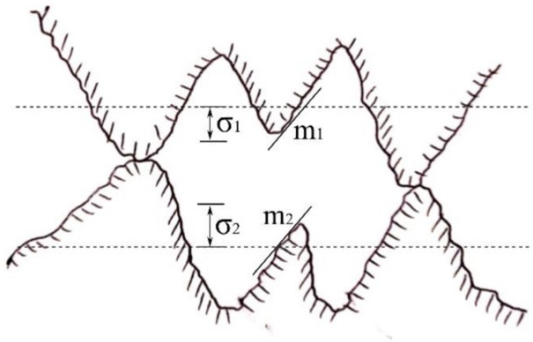

Figure 3.2: Contact of two rough surfaces at the microscopic level, displaying the surface roughness, σ and slope is asperity, m on each surface; from [47].

in equation 3.3: k_s corresponds to the thermal conductivity of the material, p_{app} to the applied pressure, and H_c to the surface microhardness. A and B are numerical constants, and their values from different models are listed in the table 3.1 proposed by Dhuley [47].

3.2.2 Thermal boundary resistance: temperature dependence

The other component is related to the interaction of the heat carriers with the physical boundary of the touching bodies. At ambient temperature, this contribution is insignificant or negligible; however, at cryogenic temperatures, it becomes significant [47]. Thermal

boundary resistance, is a phenomenon that occurs at the interface between two materials where heat carriers (phonons or electrons) encounter a physical boundary. When these heat carriers hit the interface, they can either reflect back or transmit across to the other side. Since the probability of transmission is often less than perfect, this leads to an additional resistance to heat flow.
At low temperatures, phonon wavelengths are large compared to surface roughness. In this case, phonons tend to follow the Acoustic Mismatch Model (AMM), where the heat carriers transmit in a more specular way, reflecting off the interface like light off a mirror. However, as temperatures increase and phonon wavelengths become comparable to the surface roughness, the Diffuse Mismatch Model (DMM) becomes more applicable. This model assumes that phonons transmit across the interface in a diffuse manner, much like light scattering off a rough surface. The difference between the models is shown in figure 3.3.

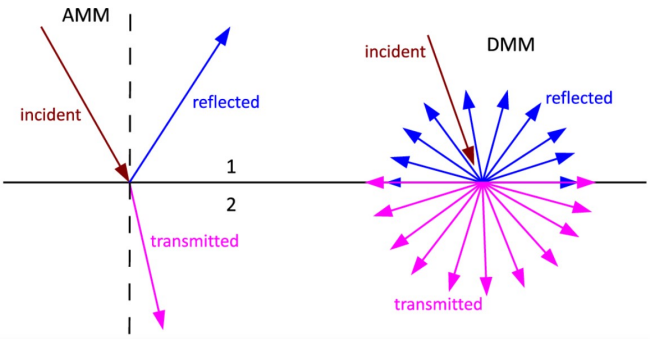

Figure 3.3: Schematic of specular and diffuse scattering assumptions in the acoustic and diffuse mismatch models respectively; from [48].

The governing equation for the heat flux across an interface takes into account the principles of energy balance and the transmission probability of heat carriers. In equation 3.3, are present: the temperarure , $\left(T^{-1}\right)$, and the pressure $\left(\frac{p_{app}}{H_c}\right)$ dependence, E_F the energy of electrons at Fermi level, n_e the density of conduction electrons, and v_F the heat carrier velocity.

4 Measurement settings

In the following paragraph, a brief description is provided of the equipment used to determine the properties of the analyzed components, their manufacturing, and the procedures to determine the thermal contact resistance. The DynaCool system, specifically the Thermal Transport Option (TTO), enables the measurement of various sample properties. In particular, it allows for thermal conductivity measurements, from which thermal resistance can be derived using a steady-state four-point measurement configuration. This setup includes two thermometers, one heater, and a heat sink. The analyzed components consist of soldered tape stacks, unsoldered tape stacks, and BRAST braids.

4.1 Measurement Instruments

4.1.1 Dynacool

The Quantum Design DynaCool is a device designed to measure multiple physical characteristics of a sample, while regulating the environmental conditions affecting the sample. The PPMS (Physical Property Measurement System) DynaCool employs a single two-stage Pulse Tube cooler to cool down the temperature in both the superconducting magnet and the temperature control system, ensuring a low-vibration setting for sample measurements. It provides consistent low-temperature and magnetic field regulation [49].
The features of the used DynaCool enable operation:

- in a temperature range between 1.8 K and 400 K;
- a magnetic field of 9 T;
- an high-vacuum enviroment $< 10^{-4}$ Torr.

The PPMS can be equipped with various instruments designed to measure a wide range of physical properties.

Thermal Transport Option

In this case, the instrument used to determine the thermal properties is the Thermal Transport Option, also called TTO. The TTO allows the simultaneous measurement of both thermal and electrical properties, operating in high-vacuum conditions. It automatically calculates the uncertainty associated with the measurements. These measurements can be monitored in real-time using the *PPMSMultiVU* software.
The TTO involves the use of a sample puck, shown in figure 4.1, which plugs into the socket at the bottom of the PPMS sample chamber. There are the shoe assemblies, including

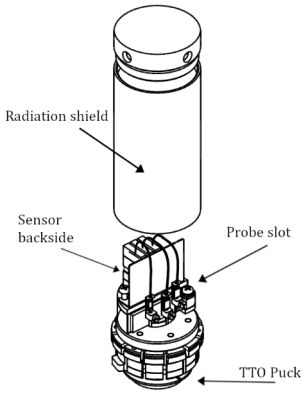

Figure 4.1: TTO Puck with Radiation Shield, from [49].

two temperature shoes and one heater shoe. They are shielded by a copper shield plate, which is placed between the board sockets and the sample stage to minimize radiation effects. The sample is connected through a coldfoot, which acts as a thermal sink for the sample, so good thermal contact is fundamental. A copper isothermal radiation shield is screwed into the base of the puck and is designed to minimize radiation losses from the sample.
The figure 4.2 shows a sample mounted in the TTO. The measurements are performed in

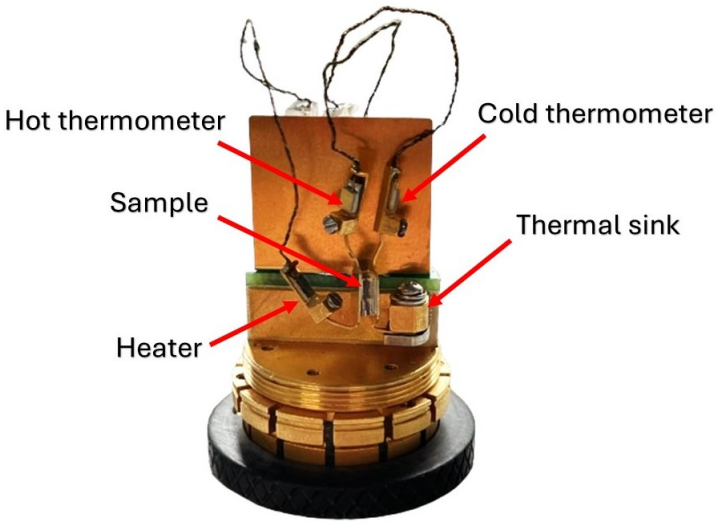

Figure 4.2: Example of a sample with thermometers and heater connected.

steady-state measurement mode, in which the system first waits for thermal equilibrium at a specified temperature. Subsequently, the sample is heated using a constant heat flux from the heater. After reaching thermal equilibrium again, the temperature gradient is measured by the Cernox thermometers.

4.1.2 Strain measurement using Wheatstone bridge

The unsoldered samples are analyzed under specific pressure to examine the effect of pressure on the thermal properties of the various configurations. To achieve this, a copper frame was used. Its shape, as shown in figure 4.3, allows the materials to be housed within it for analysis. At the lower part of the frame, a flange is inserted, enabling the frame to be

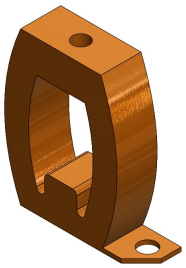

Figure 4.3: CAD of the used copper frame.

attached to the TTO. On the upper part, there is a hole in which a screw has been inserted, allowing the samples to be fixed and a specific force to be applied. The screw is made of *Kuprodur*, a copper alloy that combines the excellent thermal and electrical properties of copper with enhanced mechanical properties. The applied force is regulated by tightening the screw and measured using the strain gauges, attached to both the inner and outer parts of the frame, and connected to form a full Wheatstone bridge circuit. The setup is shown in figure 4.4.

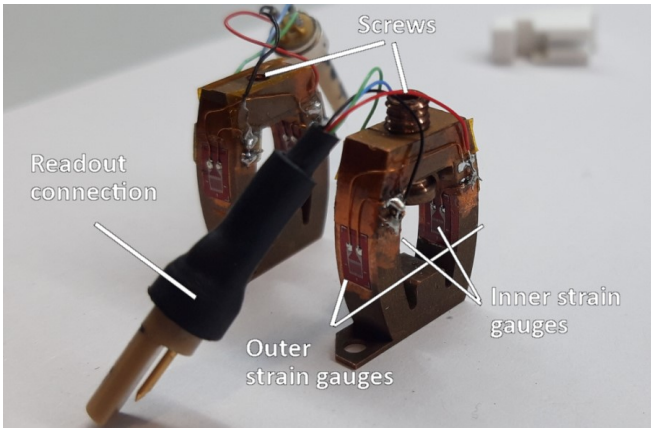

Figure 4.4: Two copper frame, equipped with strain gauges in the inner and outer part, with the readout connection to get the results on the applied force.

A Wheatstone bridge is circuit based on the presence of four resistive legs, which in this case correspond to the strain gauges. Applying a force to the frame causes a change in the dimensions of the strain gauges, this lead to a change in resistance of the gauges. Measuring the change in resistance allow to determine the applied force, with an accuracy of 0.1 N. Before use, the frame was calibrated at room and cryogenic temperatures.

4.2 Sample preparation

In this study, different types of contacts were analyzed to understand their properties under various conditions. For some types of contacts, the analysis is performed on cable segments to obtain the datas. In other cases, specific samples were constructed to measure their properties.

4.2.1 Soldered stacks

In the previous paragraph 2.2.3, the VIPER cable design is proposed, characterized by the presence of HTS soldered stacks. With the aim of replicating the soldered stacks of the VIPER cable, various processes were carried out. VIPER cables are characterized by the presence of 4 mm YBCO tapes, soldered together. Two different types of HTS tapes were used, both based on the presence of YBCO as superconductive material, which differ from each other in the thickness of their layers, the difference are shown in table 4.1.

Table 4.1: Different thicknesses of the layers in HTS tapes.

Type of HTS	Substrate thickness (both with Hastelloy C-276)	Silver thickness	Copper thickness
Type 1	60 µm	2 µm	20 µm
Type 2	38 µm	3 µm	20 µm

The first treatment performed on half of the analyzed samples consisted of placing them in a solution of water and citric acid, heated to approximately 80^{o}C, with the aim of removing oxides from the surface of the tapes. This process was carried out to assess the influence of oxide layers on contact resistance and to evaluate potential adjustments to the cable manufacturing process. Afterwards, the tapes were coated on both sides with a *SnPb* solder and cut into 4 mm sections. The cut plates were then stacked and placed in an oven at 300°C. A slight pressure was applied to the central section to facilitate the removal of excess solder, removed using abrasive paper, the result of the process is shown in figure 4.5 and 4.6.

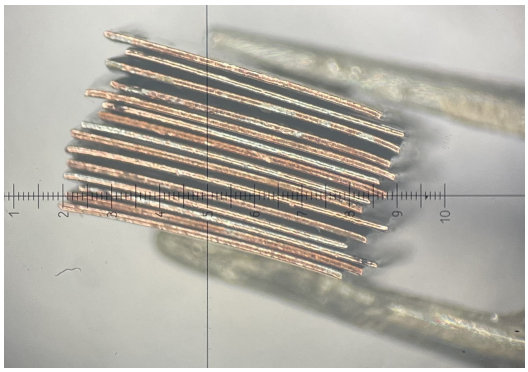

Figure 4.5: Stack before the heat treatment.

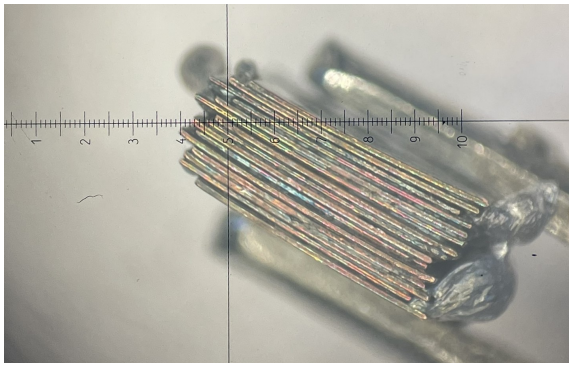

Figure 4.6: Stack after the heat treatment.

At the end, using very fine abrasive paper, the surfaces were smoothed. A microscopic view of different samples is shown in the figure 4.7.

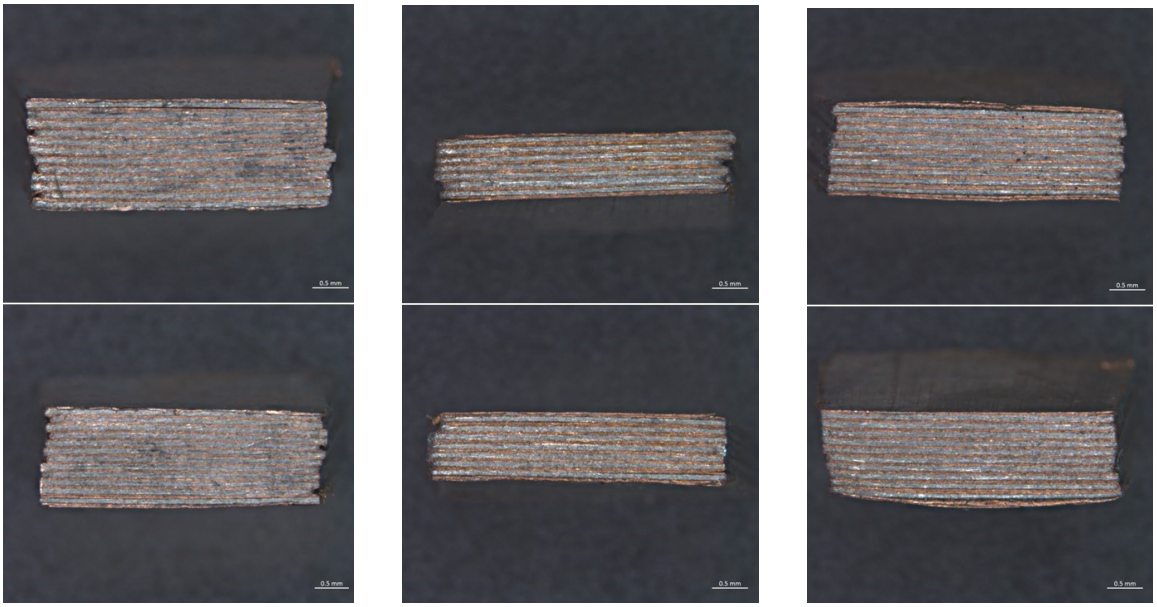

Figure 4.7: Microscopic view of different stack of soldered tapes.

After homogenizing the surfaces of the soldered tapes stacks, two plates were attached to the surfaces of the stack using a silver epoxy, *EPO-TEK® H20E*, which is characterized by its high thermal conductivity. This preparation is necessary to proceed with the measurement of thermal properties using the TTO. Figure 4.8 shows the sample ready to be installed in the TTO for measuring thermal conductance.

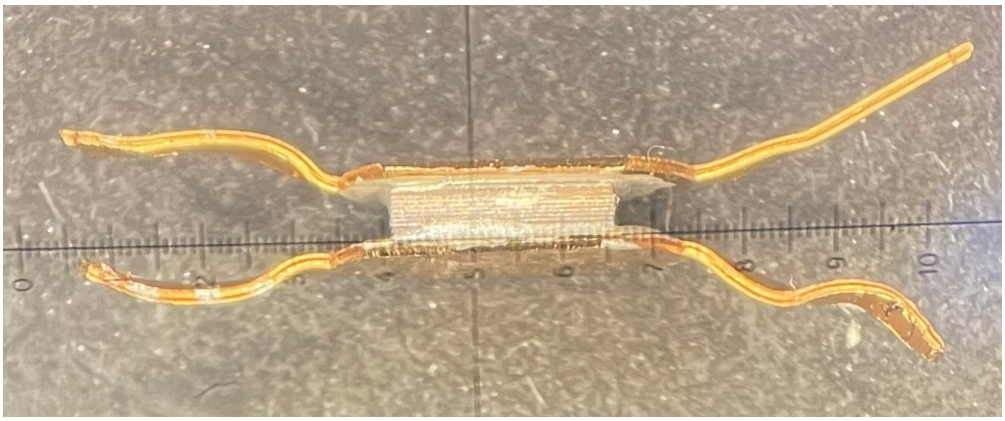

Figure 4.8: Glued sample ready to be installed in the TTO.

4.2.2 Unsoldered stacks

The assembly process of unsoldered stacks involves fewer steps. An example of such stacks includes those used for analyzing the thermal properties of SECAS cables proposed by ENEA, which are based on the use of BRAST sub-units. As previously described in the section 2.2.4, the superconducting tapes are assembled in a stack within a copper braid.

To simulate the quench conditions within the HTS tapes sub-units, analyses were conducted under various configurations in the Dynacool. To evaluate the thermal properties of the tapes stack, the superconducting wires were cut into 4 mm × 4 mm tapes using laser cutting, in order to prevent deformation of the plates. After sectioning the wires, the tapes were placed inside the copper frame using a stack mold to ensure proper alignment of the tapes. A CAD model of the stack mold is shown in figure 4.10. Following the insertion

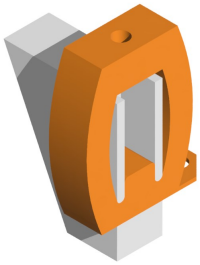

Figure 4.9: 3D CAD of the stack mold, used for 4 mm × 4 mm tapes.

into the stack mold, the tapes, the copper plates used for connecting the TTO sensors, and the copper blocks were placed in the copper frame and secured using screws, as shown in figure . The applied pressure was measured using the procedures described previously, in section 4.1.2.

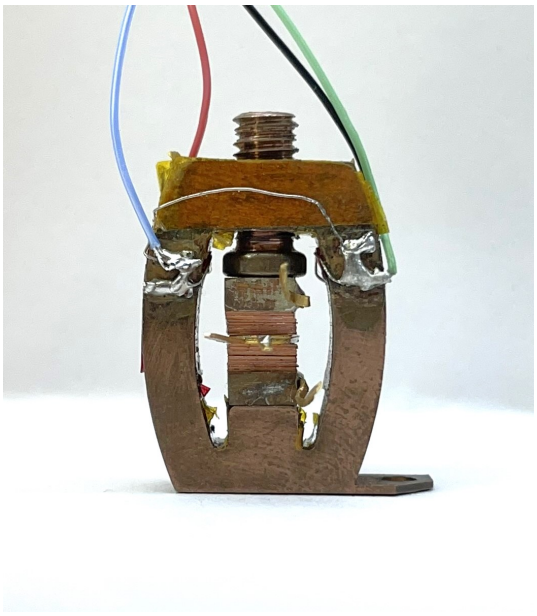

Figure 4.10: Unsoldered stack ready to be installed in the TTO.

4.2.3 BRAST cable

The preparation of the sample for determining the thermal properties of the BRAST cable starts by cutting the BRAST strand into 4 mm sections. Special care was taken during this process to avoid damaging the external braid.
To simulate the quench condition within the the BRAST sub-units, a copper plate was inserted, equipped with two contacts in order to connect the heater and the hot thermometer.
The component was inserted into the copper frame, placed between two copper blocks to which contacts were connected, enabling the link with the cold thermometer, as shown in figure 4.11. Additionally, as with the previous sample, the sub-unit of the braid was secured using a screw.

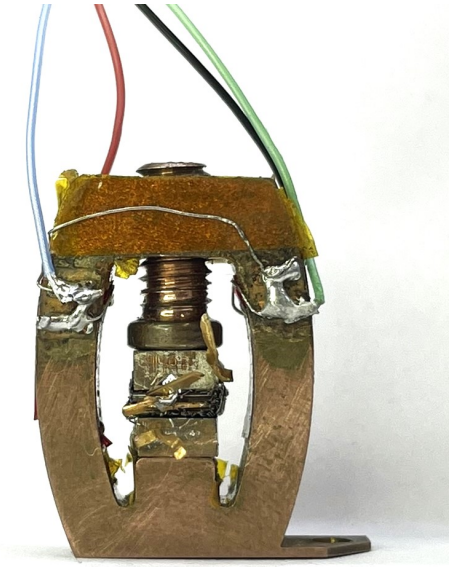

Figure 4.11: BRAST sub-unit sample ready to be installed in the TTO.

4.3 Measurement definition

This section outlines the methodology used to analyze the data obtained from measurements performed with the DynaCool system. Specifically, for the different components studied, the data were processed to derive the results presented in the following chapter, accounting for the propagation of error associated with the various measurements.

4.3.1 Soldered stacks

The soldered stack is schematically illustrated in figure 4.12. From the analysis outputs, the temperature difference of the hot and cold thermometers (ΔT) [K] and the heater power P [W] were considered. Thermal resistance was then determined as the ratio of

these two values, and subsequently normalized by the number of tapes and the surface area, as follows:

$$R_{TC,soldered} = \frac{\Delta T \cdot A}{P \cdot n_{tapes}} \tag{4.1}$$

where A is the contact area and n_{tapes} is the number of tapes per stack. The analyzed value takes into account the thermal resistance of the tape itself and the contact resistance, characterized by the presence of soldering.

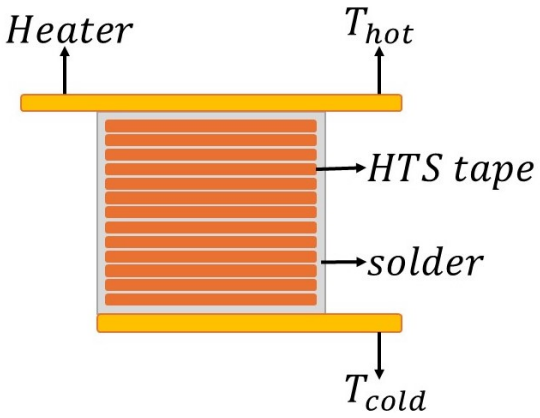

Figure 4.12: Schematic view of the soldered stack sample.

All the samples properties are shown in table 4.2, where type 1 and type 2 refer to the different materials defined in the table 4.1.

Table 4.2: Analysed soldered samples properties.

Sample name	Type of HTS	Acid citric treatment	Contact area $[cm^2]$	Number of tapes
1	Type 1	YES	0.1734	14
2	Type 1	NO	0.1681	9
3	Type 1	YES	0.1658	12
4	Type 1	NO	0.1597	8
5	Type 2	YES	0.1376	7
6	Type 2	NO	0.1539	10
7	Type 2	NO	0.1402	10
8	Type 2	YES	0.1350	6

4.3.2 Unsoldered stacks

Also for the unsoldered stacks a schematic is provided in order to visualize the connections within the TTO, as shown in figure 4.13.
In the case of these samples, the thermal resistance is characterized by several contributions, which are:

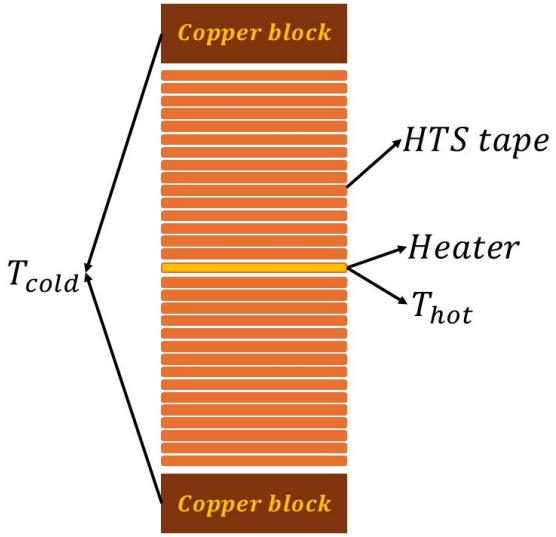

Figure 4.13: Schematic view of the unsoldered stack sample.

- the copper block to which the thermometer is connected,
- the contact between the copper block and the tape,
- the tape resistance itself,
- the contact between the tapes,
- the copper plate to which the thermometer and the heater are connected.

The electrical schematic, highlighting the various contributions in series, is shown in the figure 4.14.

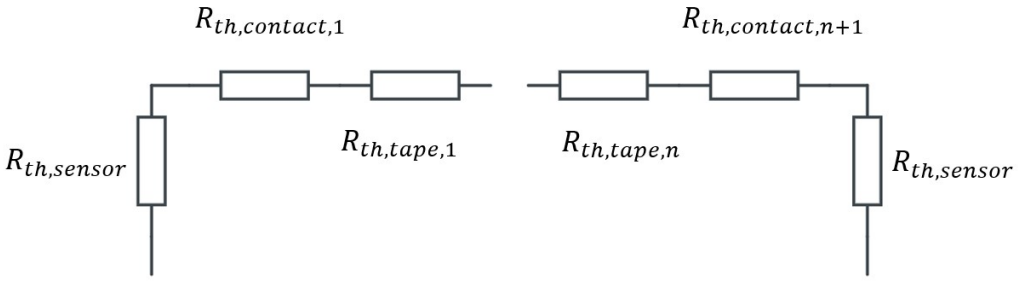

Figure 4.14: Electrical circuit equivalent of the thermal resistance model for unsoldered tapes.

The objective is to determine the thermal contact resistance between the tapes but, it is not possible to separate this value from that of the tapes themselves. Therefore, the final value shown will be the sum of both contributions. The contribution to the total thermal resistance from the copper blocks and the sensors is significantly lower, by several orders of

magnitude with respect to the total one, and is therefore neglected in the calculation. Due to the configuration of the sensors and heater, the heater power was splitted by two before determining the thermal contact resistance, to account for the symmetric distribution of power in both the top and bottom directions. The results will therefore be presented for both stacks, top and bottom, for every temperature and pressure value.

4.3.3 BRAST cable

For the BRAST cable, the thermal contact resistance, based on the configuration schematized in the figure 4.15, requires subtracting the contribution from the tapes, computed with the unsoldered stack. In this case, the evaluated thermal contact resistance is through the braid, from the top or bottom of the tape to the copper block.

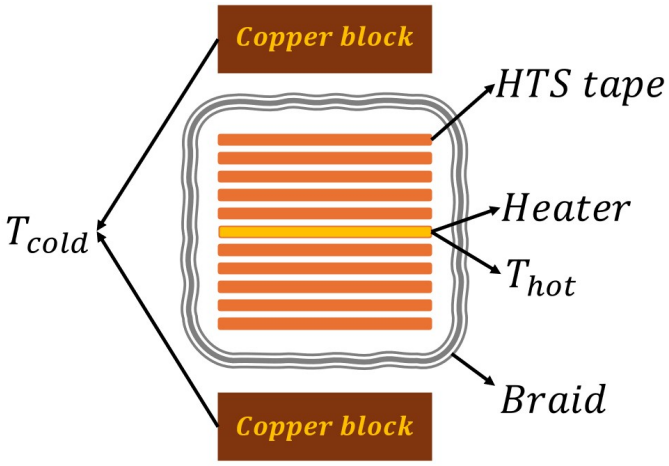

Figure 4.15: Schematic view of the BRAST cable sample.

In figure 4.15 the electrical schematic, with the contributes to the thermal resistance in series, is shown. In this case as well, the thermal contact resistance contribution from the

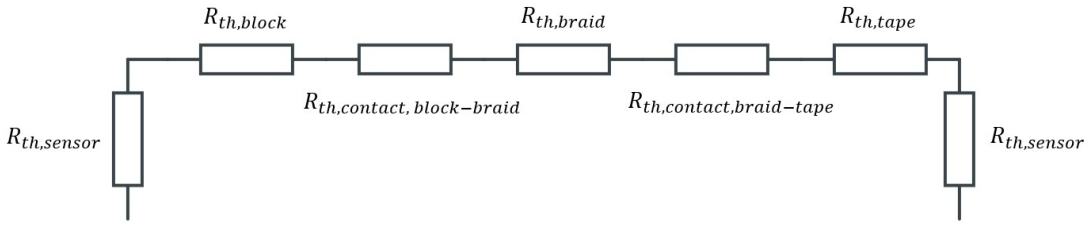

Figure 4.16: Electrical circuit equivalent of the thermal resistance model for BRAST braid.

copper block and sensors was an order of magnitude lower compared to the total resistance, and was therefore neglected. Thus, the thermal resistance value take into account the contributions from the contact between the copper block and the braid, the resistance of the braid itself, and the contact between the tape and the braid. The power was split by two to take into account the symmetric distribution of the power in the sample.

4.4 Uncertainty analysis

In this section, the analysis regarding the propagation of uncertainty in relation to the obtained results is presented. There are various sources of uncertainty that need to be taken into consideration, and they are explained in the following sections.

4.4.1 Source of of Uncertainty

To ensure the validity of the proposed results, the calculation related to uncertainty propagation was performed. There are several sources of uncertainty, and this section outlines the method by which this analysis was conducted.

Contact area

The contact area is related to the size of the tapes, which are ideally characterized by a 4 mm × 4 mm surface. Each tape, and consequently each stack, was measured with a digital caliber prior to each analysis in the DynaCool. Six measurements were taken on each side of the tape, and the final result is given by the arithmetic mean of the six measurements. The uncertainty in the contact area was evaluated as follow by equation 4.2:

$$u(A) = \frac{1}{2}[A_{max} - Amin] \tag{4.2}$$

where $A_{\max}$ corresponds to the largest area based on the longest measured sides, and $A_{\min}$ to the smallest area based on the shortest measured sides.

Thermal resistance

From the Thermal Transport specification [49], it is possible to determine the accuracy of the value of the 5% over the measured values for the thermal conductivity. Thus, the same percentage was applied to the thermal resistance.

Sample Temperature

Temperature measurements are taken using Cernox® sensors. Inside the DynaCool system, the temperature is measured by averaging the sum of both hot and cold temperatures before and during the measurement, dividing by four. Based on the technical specifications of the sensors [50], it is possible to determine the accuracy of measurements across different temperature ranges. The lower the temperature, the higher the sensor accuracy. To be conservative, an uncertainty of ±40 mK is proposed for temperatures measured above 100 K, and ±15 mK for temperatures below 100 K.

4.4.2 Formulation of Uncertainty Propagation

The error propagation calculation for the measurements was determined for each configuration using MATLAB. Starting from the equation

$$R_{TC} = \frac{\Delta T \cdot A}{W \cdot N_{tapes}} \tag{4.3}$$

the error propagation can be calculated as follows, for the soldered and unsoldered stacks:

$$u(R_{TC}) = R_{TC}\sqrt{\left(\frac{u(A)}{A}\right)^2 + \left(\frac{u(T)}{T}\right)^2 + \left(\frac{u(R_{measured})}{R_{measured}}\right)^2} \tag{4.4}$$

where $u(\Delta T)$ corresponds to the uncertainty in the sample temperature, $u(A)$ corresponds to the uncertainty in the contact area, $u(R_{measured})$ corresponds to the uncertainty on the thermal resistance measurement.
As for the thermal contact resistance between the braid and copper in the BRAST cable, an additional contribution must be added to the formula, accounting for the subtraction of the number of tapes times the uncertainty in the unsoldered tapes from the measured value.

5 Datas analysis and results

In this section, there are the results obtained for the different samples, with a specific focus on the variation of thermal contact resistance as a function of temperature for all three types of samples analyzed. Additionally, for the unsoldered tapes and the BRAST braid samples, there are also an analysis of the variation in thermal contact resistance as a function of the applied force.

5.1 Soldered stack

Eight different samples of soldered tapes were analyzed. The samples consist of two distinct types of superconducting materials, each characterized by layers of different thicknesses. In this section, the materials will be referred to as Type 1 and Type 2, as previously defined in the corresponding table 4.1.
By analyzing the thermal contact resistances of the four different samples of Type 1 material, it can be observed, by comparing the results shown in figure 5.1 , how the treatment of the tapes with citric acid to remove surface oxides lowered the thermal contact resistance. Even considering the lower thermal contact resistance values for the two different treatments, the trend in both graphs is similar. Both are characterized by higher thermal resistances at cryogenic temperatures. As the temperature increases, the thermal contact resistance decreases in both cases, tending to converge at temperatures above 100 K.

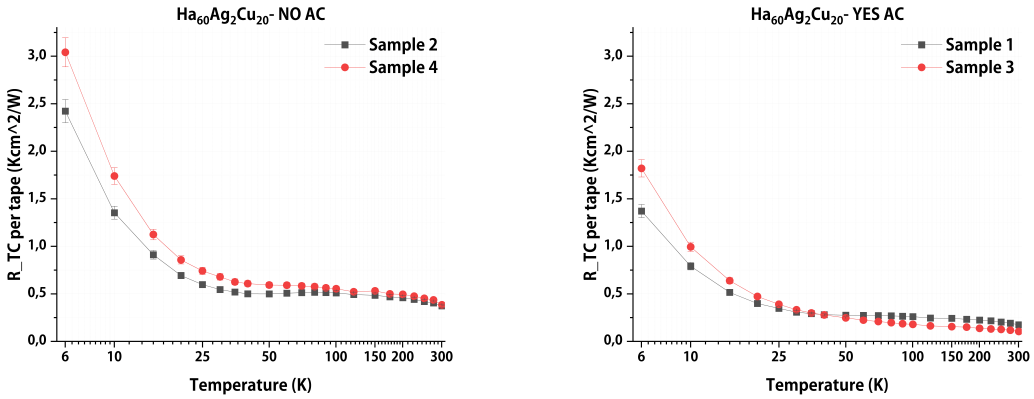

Figure 5.1: Type 1 HTS soldered tapes thermal contact resistance at different temperatures, untreated (left) and treated (right) with acid citric

A similar result was obtained for the Type 2 material samples. In this case as well, the

samples treated with citric acid showed lower thermal contact resistance compared to the untreated samples, as shown in the figure 5.2.

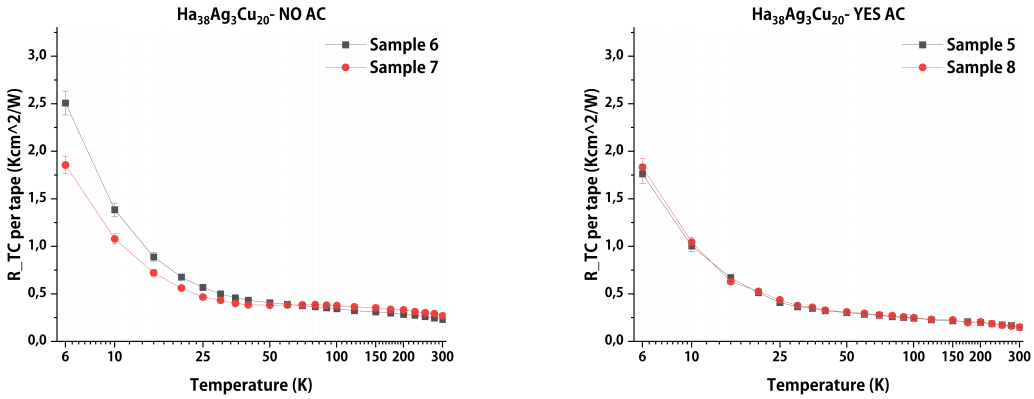

Figure 5.2: Type 2 HTS soldered tapes thermal contact resistance at different temperatures, untreated (left) and treated (right) with acid citric.

In both figures 5.1 and 5.2, it is seen the samples characterized by the same type of material but a different number of tapes, despite the normalization performed per number of tapes, exhibit slightly different thermal contact resistances. This behavior could be related to the soldering process, which was performed manually. The manual nature of the process may introduce slight variations in the quality of the sample, such as uneven solder distribution or inconsistent pressure application points in the oven, leading to small differences in thermal contact performance between the samples.

5.2 Unsoldered stack

In the case of the unsoldered stacks, measurements were taken under different applied forces to assess the variation in thermal contact resistance as a function not only of temperature but also of pressure, which as well known, is given by the ratio between the applied force and the contact surface area. Since the stacks of tapes are not soldered, applying higher pressures results in larger contact surfaces. Therefore, based on our experimental analysis, we expect that an increase in the applied pressure will lead to a decrease in thermal contact resistance.

5.2.1 Temperature dependence

The results of the measurements are shown in figure 5.3 where the thermal contact resistance of unsoldered tapes across a range of temperatures is shown, under varying applied normal forces: 50 N, 100 N, 150 N, and 200 N. For every temperature and pressure value the measurement was performed two times: for upper and lower stacks separately. The results show a steep decrease in thermal contact resistance at low temperatures (below 25 K), stabilizing as temperature increases. Higher applied forces appear to reduce the

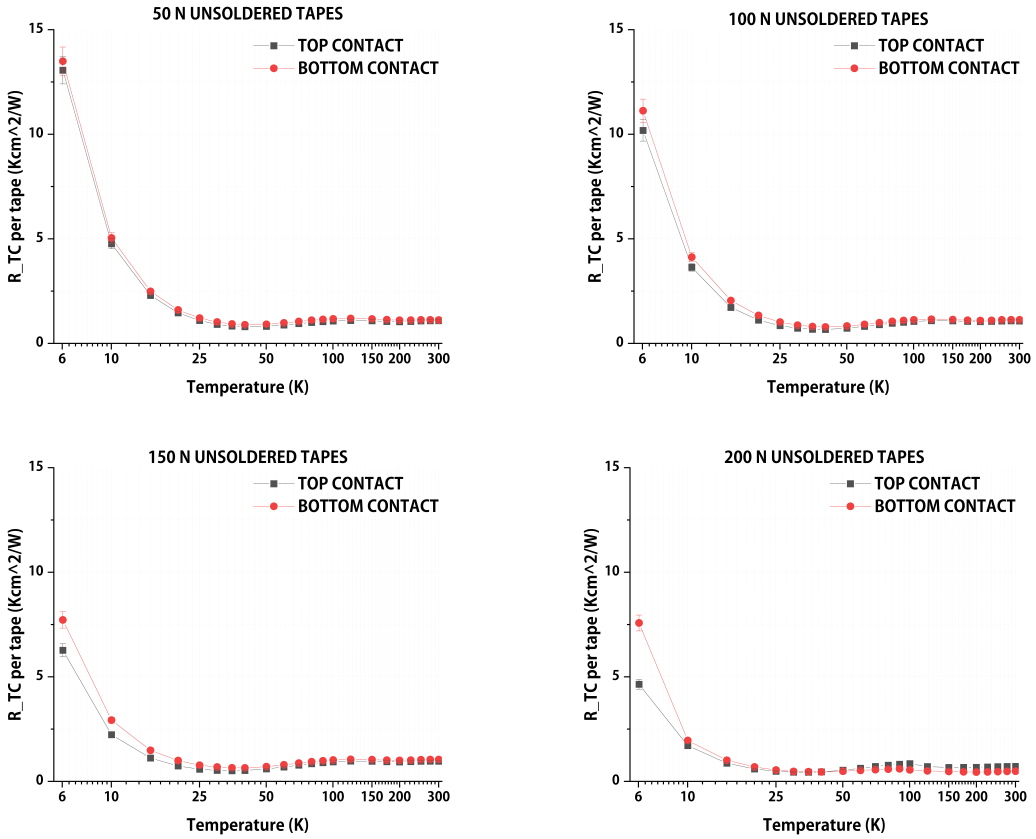

Figure 5.3: Unsoldered HTS tapes thermal contact resistance at different temperatures, with 50 N (top-left), 100 N (top-right), 150 N (down-left) and 200 N (down-right) applied.

contact resistance, especially at lower temperatures. The unsoldered tapes are characterized by higher thermal contact resistance values at cryogenic temperatures, with a corresponding decrease as the temperature increases. The trends are similar to those observed in the soldered samples, but the values are significantly different. As shown in figures 5.1, 5.2 and 5.3, the maximum thermal contact resistance for the unsoldered tapes reaches approximately 13.5 $\frac{Kcm^2}{K}$, whereas in the case of the soldered tapes, the maximum recorded value was 3 $\frac{Kcm^2}{K}$. As the configurations are symmetric, it was expected from the results that, under constant pressure, both contacts would exhibit similar profiles and values of thermal contact resistance. However, as shown in figure 5.3, there are slight discrepancies between results for upper and lower stacks. While the trends of thermal contact resistance as a function of temperature are very similar, the values are slightly higher for the bottom contact. This could be attributed to the lack of perfect alignment of the tapes, indeed the bottom contact results in slightly higher thermal contact resistance. This difference between the analyzed values for the top and bottom contacts is amplified with the application of higher pressure, but this will be better illustrated in the following section.

5.2.2 Pressure dependence

The results of the thermal contact resistance behavior as a function of pressure for the unsoldered tapes stack samples are shown in figure 5.4.
The graphs show the behavior of thermal contact resistance as a function of varying force, which translates to pressure when divided by the contact surface, across multiple temperatures (6 K, 70 K, 90 K, 150 K, and 300 K). The data indicate a clear decrease in resistance with increasing applied force. As the applied force increases, the thermal contact

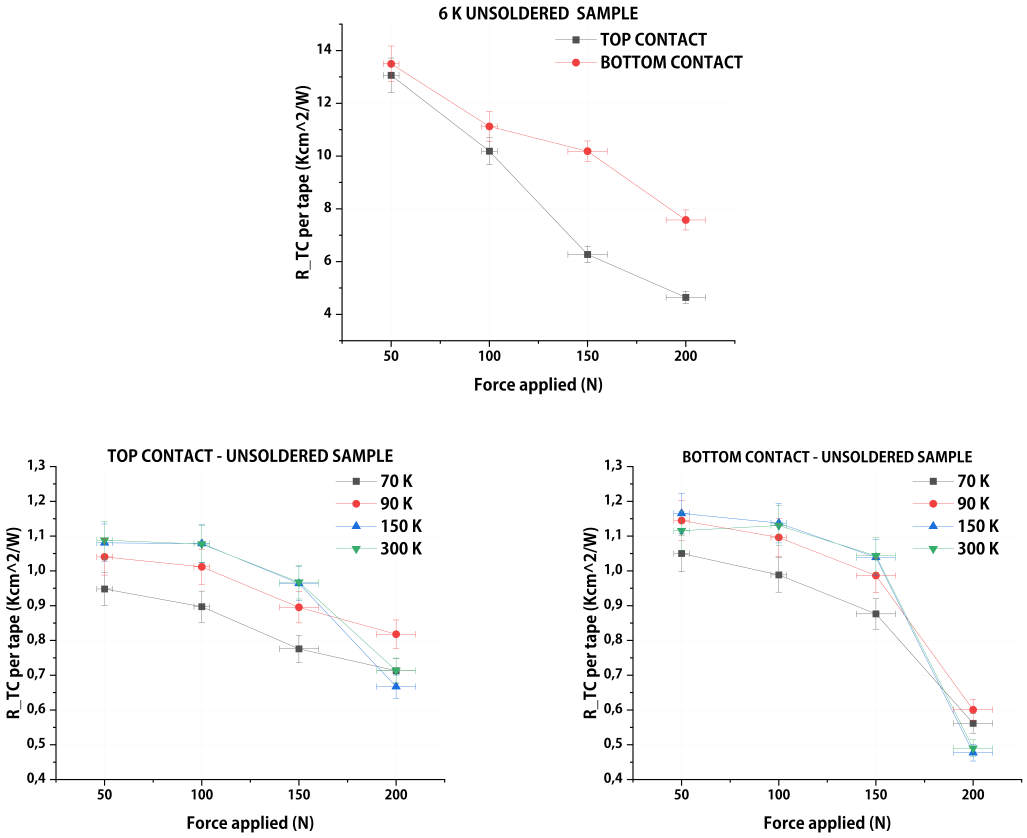

Figure 5.4: HTS soldered tapes thermal contact resistance at different forces at 6 K (top), and other operational temperatures for both top (bottom left) and bottom (bottom right) contact.

resistance decreases for both the top and bottom contacts, which is consistent with the expectation that higher pressure reduces thermal contact resistance due to increased real contact area. It is possible to observe the difference in magnitude between the values at 6 K and those at higher temperatures. This highlights the significant influence that temperature has on the properties of the materials, particularly when working at cryogenic temperatures. Furthermore, the bottom contact shows consistently higher resistance than the top contact across all applied forces, as previously stated.

5.3 BRAST braid

The analysis of the results obtained from the BRAST braid was performed in a similar way with respect to the one used for the unsoldered tapes, as mentioned in the previous section. In fact, the measured thermal contact resistance values for this sample were corrected by subtracting the contribution from the presence of 10 tapes (5 on each side, in both the top and bottom contacts) within the braid.

5.3.1 Temperature dependence

The results of the thermal contact resistance of BRAST braid at various temperatures, with different applied normal forces (50 N, 100 N, 150 N, and 200 N) are shown in figure 5.5. Each graph illustrates the resistance measured at the top and bottom configurations. The data reveal a pronounced decrease in thermal contact resistance at low temperatures (below 25 K), stabilizing as the temperature rises. The thermal contact resistance profiles exhibit trends very similar to those obtained in the previous cases. However, in this case, the difference in resistance values at cryogenic temperatures is significantly higher compared to the previously analyzed cases.

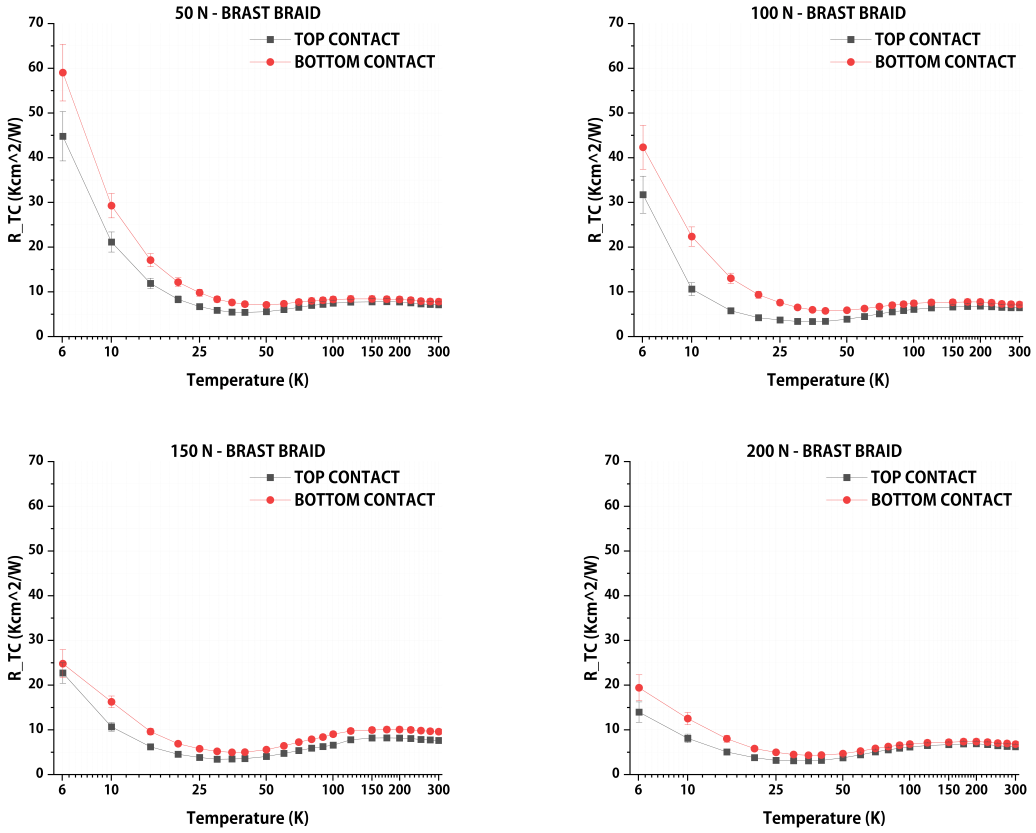

Figure 5.5: BRAST braid thermal contact resistance at different temperatures, with 50 N (top-left), 100 N (top-right), 150 N (down-left) and 200 N (down-right) applied.

This behavior is likely related to the structure of the braid surrounding the tapes. The braid is composed of fine, intertwined wires around the tapes, this allows heat to distribute not just in a unidirectional way, but throughout the entire section surrounding the tapes. Also in this case, differences between top and bottom contacts are present.

5.3.2 Pressure dependence

Figure 5.6 presents the thermal contact resistance of BRAST braid across different applied forces, starting from 50 N to 200 N, and temperatures (6 K, 70 K, 90 K, 150 K, and 300 K) for both the top and bottom contacts. 5.6

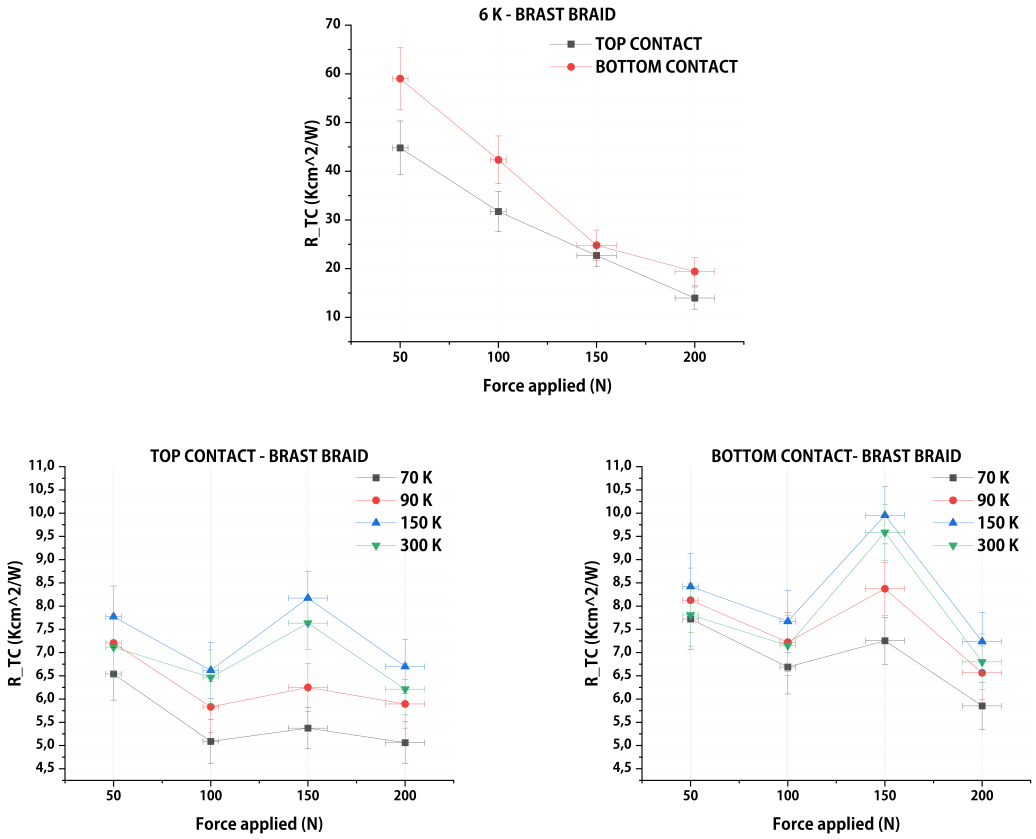

Figure 5.6: BRAST braid thermal contact resistance at different forces at 6 K (top), and other operational temperatures for both top (bottom left) and bottom (bottom right) contact.

The component at 6 K exhibits behavior consistent with the previous case: the higher the pressure, the lower the thermal contact resistance. However, this behavior is not observed at the other temperatures where resistance was evaluated. In fact, with the application of a force of 150 N, an increase in thermal contact resistance was recorded across all temperature ranges, an anomalous behavior compared to the previous cases. This behavior was observed for both the top and bottom contacts.

6 Conclusion and future analysis perspectives

This study has investigated the thermal contact resistance of different metallic surface configurations relevant to high-current HTS Cable-in-Conduit Conductors (CICC) used in large high-field magnets. The experiments were conducted on soldered, unsoldered, and BRAST braid samples across a wide range of pressures and temperatures.
The results confirm that the thermal contact resistance decreases with increasing pressure, a result of the increased real contact area between the materials. This behavior was particularly pronounced at low temperatures.
The soldered samples, especially those treated with citric acid, shown lower resistance compared to untreated and unsoldered samples, behavior related to the removal of the oxide layer. For the unsoldered samples, the influence of pressure was evident, with higher applied forces leading to noticeable reductions in thermal contact resistance. However, the observed discrepancies between the top and bottom contacts suggest the need for more precise control in the alignment and preparation of samples to achieve uniformity in results.

At 6 K, the highest thermal contact resistance values for the soldered tapes were 3.04 Wcm^2/K per tape for Type 1 without AC treatment and 1.82 Wcm^2/K per tape for Type 1 with AC treatment. For Type 2, the maximum values were 2.51 Wcm^2/K per tape without AC treatment and 1.86 Wcm^2/K per tape with AC treatment. For the unsoldered tapes, the maximum thermal contact resistance values per tape are observed with 50 N applied: 13.06 Wcm^2/K at the top contact and 13.49 Wcm^2/K at the bottom. With 100 N applied, the values are 10.18 Wcm^2/K at the top and 11.12 Wcm^2/K at the bottom. At 150 N, the top contact measures 6.27 Wcm^2/K and the bottom 7.72 Wcm^2/K. With 200 N applied, the top contact has a resistance of 4.64 Wcm^2/K, while the bottom 7.58 Wcm^2/K. The BRAST braid analysis shows higher thermal contact resistance compared to all other samples analyzed, with an unexpected result at high pressure and cryogenic temperatures, suggesting that further investigation into the internal structure and behavior of the braid is needed. At 6 K, the thermal contact resistance value is 44.79 Wcm^2/K for the top and 59.03 Wcm^2/K for the bottom, with 50 N applied. With 100 N, the recorded values are 31.73 Wcm^2/K for the top and 42.34 Wcm^2/K for the bottom. At 150 N, the values are 22.71 Wcm^2/K for the top and 24.80 Wcm^2/K for the bottom. With 200 N applied, the thermal contact resistance measures 13.97 Wcm^2/K for the top and 19.40 Wcm^2/K for the bottom.

This study provides important datas for thermal contact resistance across different configurations, however, further investigations for other contact configurations are needed. Furthermore, the research primarily investigated the effects of temperature and pressure, but several other material properties could significantly influence the thermal properties and should be examined. These include surface roughness, the thickness and width of the

tapes, and the overall microstructural integrity of the contact interfaces. Incorporating these factors into future studies could provide a more complete understanding of how thermal contact resistance behaves under various operational conditions.

Other contact configurations, particularly those involving copper or stainless steel tapes and bulk structural materials, remain to be analyzed. A comprehensive analysis of these contacts could provide further insights into optimizing heat transfer in HTS systems, which is critical for their application in fusion reactors and other high-current technologies.

In conclusion, this thesis has contributed to the knowledge of HTS CICC systems by characterizing the thermal contact resistance in some configurations.

Bibliography

[1] Dirk van Delft and Peter Kes. "The discovery of superconductivity". In: *Physics Today* 63.9 (Sept. 2010), pp. 38–43. ISSN: 0031-9228. DOI: 10.1063/1.3490499. URL: https://doi.org/10.1063/1.3490499.

[2] W. Meissner and R. Ochsenfeld. "Ein neuer Effekt bei Eintritt der Supraleitfähigkeit". In: *Naturwissenschaften* 21.44 (Nov. 1933), pp. 787–788. DOI: 10.1007/BF01504252. URL: https://doi.org/10.1007/BF01504252.

[3] Ram Gopal Sharma. *Superconductivity: Basics and applications to magnets*. Vol. 214. Springer Nature, 2021.

[4] URL: http://hyperphysics.phy-astr.gsu.edu/hbase/Solids/scbc.html.

[5] V. L. Ginzburg and L. D. Landau. "On the Theory of superconductivity". In: *Zh. Eksp. Teor. Fiz.* 20 (1950). Ed. by D. ter Haar, pp. 1064–1082. DOI: 10.1016/B978-0-08-010586-4.50035-3.

[6] J. G. Bednorz and K. A. Müller. "Possible high Tc superconductivity in the BaLaCuO system". In: *Zeitschrift für Physik B Condensed Matter* 64 (Sept. 1986), pp. 189–193. ISSN: 1431-584X. DOI: 10.1007/BF01303701. URL: https://doi.org/10.1007/BF01303701.

[7] M. K. Wu et al. "Superconductivity at 93 K in a new mixed-phase Y-Ba-Cu-O compound system at ambient pressure". In: *Phys. Rev. Lett.* 58 (9 1987), pp. 908–910. DOI: 10.1103/PhysRevLett.58.908. URL: https://link.aps.org/doi/10.1103/PhysRevLett.58.908.

[8] Annette Bussmann-Holder and Hugo Keller. "High-temperature superconductors: underlying physics and applications". In: *Zeitschrift für Naturforschung B* 75 (Nov. 2019), pp. 3–14. URL: https://doi.org/10.48550/arXiv.1911.02303.

[9] F. B. Silsbee. "A note on electrical conduction in metals at low temperatures". In: *Journal of the Washington Academy of Sciences* 6.17 (1916), pp. 597–602. ISSN: 00430439. URL: http://www.jstor.org/stable/24521242 (visited on 04/04/2024).

[10] Chao Yao and Yanwei Ma. "Superconducting materials: Challenges and opportunities for large-scale applications". In: *iScience* 24 (May 2021), p. 102541. DOI: 10.1016/j.isci.2021.102541.

[11] Chan Park and Robert L. Snyder. "Structures of High-Temperature Cuprate Superconductors". In: *Journal of the American Ceramic Society* 78.12 (1995), pp. 3171–3194. DOI: https://doi.org/10.1111/j.1151-2916.1995.tb07953.x. eprint: https://ceramics.onlinelibrary.wiley.com/doi/pdf/10.1111/j.1151-2916.1995.tb07953.x. URL: https://ceramics.onlinelibrary.wiley.com/doi/abs/10.1111/j.1151-2916.1995.tb07953.x.

[12] Yoichi Kamihara et al. “Iron-based layered superconductor: LaOFeP”. In: *Journal of the American Chemical Society* 128.31 (2006), pp. 10012–10013.

[13] G. Savini, A. C. Ferrari, and Feliciano Giustino. “First-Principles Prediction of Doped Graphane as a High-Temperature Electron-Phonon Superconductor”. In: *Phys. Rev. Lett.* 105 (3 July 2010), p. 037002. DOI: 10.1103/PhysRevLett.105.037002. URL: https://link.aps.org/doi/10.1103/PhysRevLett.105.037002.

[14] Jun Nagamatsu et al. “Superconductivity at 39K in magnesium diboride”. In: 410.6824 (Mar. 2001), pp. 63–64. DOI: 10.1038/35065039.

[15] V. I. Anisimov, D. Bukhvalov, and T. M. Rice. “Electronic structure of possible nickelate analogs to the cuprates”. In: *Phys. Rev. B* 59 (12 Mar. 1999), pp. 7901–7906. DOI: 10.1103/PhysRevB.59.7901. URL: https://link.aps.org/doi/10.1103/PhysRevB.59.7901.

[16] D. Larbalestier, A. Gurevich, and D.M. Feldmann. “High-Tc superconducting materials for electric power applications”. In: *Nature* 414 (2001), pp. 368–377. URL: https://doi.org/10.1038/35104654.

[17] V.J. Emery. “Theory of high-Tc superconductivity in oxides”. In: *Physical Review Letters* 58.26 (1987), pp. 2794–2797. DOI: 10.1103/PhysRevLett.58.2794. URL: https://www.scopus.com/inward/record.uri?eid=2-s2.0-3342896818&doi=10.1103%2fPhysRevLett.58.2794&partnerID=40&md5=f1a5df437ad96c18e8de6ec93fad9b07.

[18] P. Chaudhari et al. “Critical-current measurements in epitaxial films of $YBa_2Cu_3O_{7-x}$ compound”. In: *Phys. Rev. Lett.* 58 (25 June 1987), pp. 2684–2686. DOI: 10.1103/PhysRevLett.58.2684. URL: https://link.aps.org/doi/10.1103/PhysRevLett.58.2684.

[19] Hiroshi Maeda et al. “A New High-Tc Oxide Superconductor without a Rare Earth Element”. In: *Japanese Journal of Applied Physics* 27.2A (Feb. 1988), p. L209. DOI: 10.1143/JJAP.27.L209. URL: https://dx.doi.org/10.1143/JJAP.27.L209.

[20] A. S. EDDINGTON. “The Internal Constitution of the Stars”. In: *Nature* 20 (1920), pp. 14–20. DOI: 10.1038/106014a0. URL: https://doi.org/10.1038/106014a0.

[21] Alexander Piel et al. “An introduction to laboratory, space, and fusion plasmas”. In: *Plasma Physics* (2010).

[22] J D Lawson. “Some Criteria for a Power Producing Thermonuclear Reactor”. In: *Proceedings of the Physical Society. Section B* 70.1 (Jan. 1957), p. 6. DOI: 10.1088/0370-1301/70/1/303. URL: https://dx.doi.org/10.1088/0370-1301/70/1/303.

[23] URL: https://news.mit.edu/2018/nas-report-right-path-fusion-energy-1221.

[24] Jr. Spitzer Lyman. “The Stellarator Concept”. In: *The Physics of Fluids* 1.4 (July 1958), pp. 253–264. ISSN: 0031-9171. DOI: 10.1063/1.1705883. eprint: https://pubs.aip.org/aip/pfl/article-pdf/1/4/253/12605179/253_1_online.pdf. URL: https://doi.org/10.1063/1.1705883.

[25] URL: https://www.energyencyclopedia.com/en/nuclear-fusion.

[26] E A Azizov. “Tokamaks: from A D Sakharov to the present (the 60-year history of tokamaks)”. In: *Physics-Uspekhi* 55.2 (Feb. 2012), p. 190. DOI: 10.3367/UFNe.0182.201202j.0202. URL: https://dx.doi.org/10.3367/UFNe.0182.201202j.0202.

[27] M. Hoenig and D. Montgomery. “Dense supercritical-helium cooled superconductors for large high field stabilized magnets”. In: *IEEE Transactions on Magnetics* 11.2 (1975), pp. 569–572. DOI: 10.1109/TMAG.1975.1058601.

[28] Tsutomu Hemmi et al. “Neutron Diffraction Measurements of Internal Strain in Nb3Sn Cable-In-Conduit Conductors”. In: *IEEE Transactions on Applied Superconductivity - IEEE TRANS APPL SUPERCONDUCT* 21 (June 2011), pp. 2028–2031. DOI: 10.1109/TASC.2010.2089770.

[29] Ipsita Das, Vineet Sahoo, and V V Rao. “Structural Analysis of 2G HTS Tapes under Different Loading Conditions for HTS Power Cable using Finite Element Modeling”. In: *Physica C: Superconductivity and its Applications* 618 (2024), p. 1353771. ISSN: 0921-4534. DOI: https://doi.org/10.1016/j.physc.2020.1353771. URL: https://www.sciencedirect.com/science/article/pii/S0921453420302197.

[30] Eleni Tsotsopoulou et al. “Modelling and Fault Current Characterization of Superconducting Cable with High Temperature Superconducting Windings and Copper Stabilizer Layer”. In: *Energies* 13.24 (2020). ISSN: 1996-1073. DOI: 10.3390/en13246646. URL: https://www.mdpi.com/1996-1073/13/24/6646.

[31] Kai Wang et al. “Advances in second-generation high-temperature superconducting tapes and their applications in high-field magnets”. In: *Soft Science* 2.3 (2022). ISSN: 2769-5441. DOI: 10.20517/ss.2022.10. URL: https://www.oaepublish.com/articles/ss.2022.10.

[32] G. Celentano et al. “Design of an Industrially Feasible Twisted-Stack HTS Cable-in-Conduit Conductor for Fusion Application”. In: *IEEE Transactions on Applied Superconductivity* 24.3 (2014), pp. 1–5. DOI: 10.1109/TASC.2013.2287910.

[33] G. De Marzi et al. “Bending Tests of HTS Cable-In-Conduit Conductors for High-Field Magnet Applications”. In: *IEEE Transactions on Applied Superconductivity* 26.4 (2016), pp. 1–7. DOI: 10.1109/TASC.2016.2528501.

[34] L. Muzzi et al. “Design and Feasibility Assessment of an HTS Sector Shaped High-Current Conductor for Fusion Coils”. In: *IEEE Transactions on Applied Superconductivity* 33.5 (2023), pp. 1–6. DOI: 10.1109/TASC.2023.3236592.

[35] Michael J. Wolf et al. “HTS CroCo: A Stacked HTS Conductor Optimized for High Currents and Long-Length Production”. In: *IEEE Transactions on Applied Superconductivity* 26.2 (2016), pp. 19–24. DOI: 10.1109/TASC.2016.2521323.

[36] Daniel S. Nickel et al. “Impact of Bending on the Critical Current of HTS CrossConductors”. In: *IEEE Transactions on Applied Superconductivity* 31.5 (2021), pp. 1–4. DOI: 10.1109/TASC.2021.3076491.

[37] Michael J. Wolf et al. "Design and analysis of HTS subsize-conductors for quench investigations towards future HTS fusion magnets". In: *Cryogenics* 104 (2019), p. 102980. ISSN: 0011-2275. DOI: https://doi.org/10.1016/j.cryogenics.2019.102980. URL: https://www.sciencedirect.com/science/article/pii/S0011227519302619.

[38] Zachary S Hartwig et al. "VIPER: an industrially scalable high-current high-temperature superconductor cable". In: *Superconductor Science and Technology* 33.11 (Oct. 2020), 11LT01. DOI: 10.1088/1361-6668/abb8c0. URL: https://dx.doi.org/10.1088/1361-6668/abb8c0.

[39] T. Janowski et al. "Superconducting Devices for Power Engineering". In: *Acta Physica Polonica A* 130 (Aug. 2016), pp. 537–544. DOI: 10.12693/APhysPolA.130.537.

[40] Maxim Marchevsky. "Quench Detection and Protection for High-Temperature Superconductor Accelerator Magnets". In: *Instruments* 5.3 (2021). ISSN: 2410-390X. DOI: 10.3390/instruments5030027. URL: https://www.mdpi.com/2410-390X/5/3/27.

[41] M. A. Green. "Various Quench Protection Methods for HTS Magnets". In: *IOP Conference Series: Materials Science and Engineering* 755.1 (Mar. 2020), p. 012134. DOI: 10.1088/1757-899X/755/1/012134. URL: https://dx.doi.org/10.1088/1757-899X/755/1/012134.

[42] URL: https://indico.cern.ch/event/194284/contributions/1472819/attachments/281522/393603/TenKate_-_CAS_-Handout-Quench-Erice-2103.pdf.

[43] URL: https://indico.cern.ch/event/975584/contributions/4426212/attachments/2352492/4013509/VIPER%20structural%20modeling%20Poster.pdf.

[44] URL: https://indico.cern.ch/event/1302031/contributions/5620809/attachments/2743314/4772725/ENEA%20Actities%20on%20REBCO%20and%20IBS%20-%20AAugieri.pdf.

[45] Harry J. Sauer Jr. and J. W. Sheffield. *Thermal Contact Resistance (TCR)/Thermal Contact Conductance (TCC)*. New York, Feb. 2014. DOI: 10.1615/hedhme.a.000164. URL: https://hedhme.com/content_map/?link_id=17461&article_id=164.

[46] "THERMAL CONTACT RESISTANCE". In: *THERMOPEDIA* (2011). DOI: 10.1615/AtoZ.t.thermal_contact_resistance. URL: https://www.thermopedia.com/content/1188.

[47] R.C. Dhuley. "Pressed copper and gold-plated copper contacts at low temperatures – A review of thermal contact resistance". In: *Cryogenics* 101 (2019), pp. 111–124. ISSN: 0011-2275. DOI: https://doi.org/10.1016/j.cryogenics.2019.06.008. URL: https://www.sciencedirect.com/science/article/pii/S0011227519300943.

[48] Sridhar Sadasivam et al. "THE ATOMISTIC GREEN'S FUNCTION METHOD FOR INTERFACIAL PHONON TRANSPORT". In: *Annual Review of Heat Transfer* 17 (2014), pp. 89–145. URL: https://api.semanticscholar.org/CorpusID:38416474.

[49] URL: https://qdusa.com/products/dynacool.html.

[50] URL: https://www.lakeshore.com/products/categories/specification/temperature-products/cryogenic-temperature-sensors/cernox.